



The Geochemistry of Magnetite and Apatite from the El Laco Iron Oxide-Apatite Deposit, Chile: Implications for Ore Genesis

Nikita L. La Cruz,^{1,2,†} J. Tomás Ovalle,^{3,4} Adam C. Simon,¹ Brian A. Konecke,^{1,5} Fernando Barra,^{3,4} Martin Reich,^{3,4} Mathieu Leisen,^{3,4} and Tristan M. Childress¹

¹*Department of Earth and Environmental Sciences, University of Michigan, Ann Arbor, Michigan 48109*

²*Geological Services Division, Guyana Geology and Mines Commission, Georgetown, Guyana*

³*Department of Geology and Andean Geothermal Center of Excellence (CEGA), Faculty of Physical and Mathematical Sciences (FCFM), Universidad de Chile, Santiago 08370450, Chile*

⁴*Millennium Nucleus for Metal Tracing Along Subduction, Universidad de Chile, Santiago 08370450, Chile*

⁵*Astromaterials Research and Exploration Science (ARES), NASA, Johnson Space Center, Houston, Texas 77058*

Abstract

The textures of outcrop and near-surface exposures of the massive magnetite orebodies (>90 vol % magnetite) at the Plio-Pleistocene El Laco iron oxide-apatite (IOA) deposit in northern Chile are similar to basaltic lava flows and have compositions that overlap high- and low-temperature hydrothermal magnetite. Existing models—liquid immiscibility and complete metasomatic replacement of andesitic lava flows—attempt to explain the genesis of the orebodies by entirely igneous or entirely hydrothermal processes. Importantly, those models were developed by studying only near-surface and outcrop samples. Here, we present the results of a comprehensive study of samples from outcrop and drill core that require a new model for the evolution of the El Laco ore deposit. Backscattered electron (BSE) imaging, electron probe microanalysis (EPMA), and laser ablation inductively coupled plasma mass spectrometry (LA-ICP-MS) were used to investigate the textural and compositional variability of magnetite and apatite from surface and drill core samples in order to obtain a holistic understanding of textures and compositions laterally and vertically through the orebodies. Magnetite was analyzed from 39 surface samples from five orebodies (Cristales Grandes, Rodados Negros, San Vicente Alto, Laco Norte, and Laco Sur) and 47 drill core samples from three orebodies (Laco Norte, Laco Sur, and Extensión Laco Sur). The geochemistry of apatite from eight surface samples from three orebodies (Cristales Grandes, Rodados Negros, and Laco Sur) was investigated. Minor and trace element compositions of magnetite in these samples are similar to magnetite from igneous rocks and magmatic-hydrothermal systems. Magnetite grains from deeper zones of the orebodies contain >1 wt % titanium, as well as ilmenite oxyexsolution lamellae and interstitial ilmenite. The ilmenite oxyexsolution lamellae, interstitial ilmenite, and igneous-like trace element concentrations in titanomagnetite from the deeper parts of the orebodies are consistent with original crystallization of titanomagnetite from silicate melt or high-temperature magmatic-hydrothermal fluid. The systematic decrease of trace element concentrations in magnetite from intermediate to shallow depths is consistent with progressive growth of magnetite from a cooling magmatic-hydrothermal fluid. Apatite grains from surface outcrops are F rich (typically >3 wt %) and have compositions that overlap igneous and magmatic-hydrothermal apatite. Magnetite and fluorapatite grains contain mineral inclusions (e.g., monazite and thorite) that evince syn- or postmineralization metasomatic alteration. Magnetite grains commonly meet at triple junctions, which preserve evidence for reequilibration of the ore minerals with hydrothermal fluid during or after mineralization. The data presented here are consistent with genesis of the El Laco orebodies via shallow emplacement and eruption of magnetite-bearing magmatic-hydrothermal fluid suspensions that were mobilized by decompression-induced collapse of the volcanic edifice. The ore-forming magnetite-fluid suspension would have rheological properties similar to basaltic lava flows, which explains the textures and presence of cavities and gas escape tubes in surface outcrops.

Introduction

Kiruna-type iron oxide-apatite (IOA) deposits are an important source of iron and a potentially important source of rare earth elements (REE). Iron oxide-apatite deposits are found in districts globally and are commonly hosted in volcanic and plutonic rocks in convergent margins and rift-related environments (Williams et al., 2005; Groves et al., 2010; Barton, 2013; Simon et al., 2018). El Laco, the youngest known and best-preserved IOA deposit, is one of the most enigmatic ore deposits on Earth. El Laco has perplexed geologists since Park

(1961) first described textures of the surficially exposed orebodies as resembling a magnetite “flow.”

Currently, there are three hypotheses for the formation of the El Laco orebodies. One hypothesis invokes crystallization of magnetite from erupted H₂O-saturated, Cl-, S-, F-rich iron oxide magma that formed as a result of liquid immiscibility (Nyström and Henríquez, 1994; Naslund et al., 2002; Henríquez et al., 2003; Naranjo et al., 2010; Tornos et al., 2016; Velasco et al., 2016; Broughm et al., 2017; Xie et al., 2019). A second hypothesis invokes complete, texture-preserving replacement of andesitic volcanic and hypabyssal rocks by magnetite that precipitated from a hydrothermal fluid (Rhodes and Oreskes, 1995, 1999; Rhodes et al., 1999;

[†]Corresponding author: e-mail, nlacruz@umich.edu

Sillitoe and Burrows, 2002; Dare et al., 2015). A third, hybrid hypothesis invokes early crystallization of magnetite microlites from a silicate melt followed by exsolution of a magmatic volatile phase that wets and attaches to the magnetite microlites forming a magnetite-rich suspension within a silicate magma. This suspension ascends and is later injected into the crust and vented to the surface owing to the collapse of the volcanic edifice (Ovalle et al., 2018). This third hypothesized process results in the formation of large breccia bodies at depth and massive magnetite bodies at shallow levels that exhibit igneous and hydrothermal textural and geochemical features, respectively.

In this study, we have attempted to distinguish among these alternative models by evaluating textural and chemical characteristics of magnetite, the primary ore mineral, and apatite, a common gangue mineral at El Lago. Magnetite samples investigated in the study came from surface outcrops at Cris-

tales Grandes (CG), Rodados Negros (RN), San Vicente Alto (SVA), Laco Norte (LN), and Laco Sur (LS), and from drill cores from the Laco Norte (LN), Laco Sur (LS), and Extensión Laco Sur orebodies. This study is the second one to incorporate samples from drill core at El Lago (Ovalle et al., 2018). Apatite samples used in this study came from outcrop samples at Cristales Grandes (CG), Rodados Negros (RN), and Laco Sur (LS). The geochemistry and textures of magnetite and apatite reveal that the orebodies formed by a combination of magmatic and magmatic-hydrothermal processes that is consistent with the hybrid magmatic/magmatic-hydrothermal model proposed by Ovalle et al. (2018).

Geologic Background

The El Lago Volcanic Complex and associated IOA deposit are located east of the active volcanic arc in the Central Andes along the western South American continental margin (Fig. 1A;

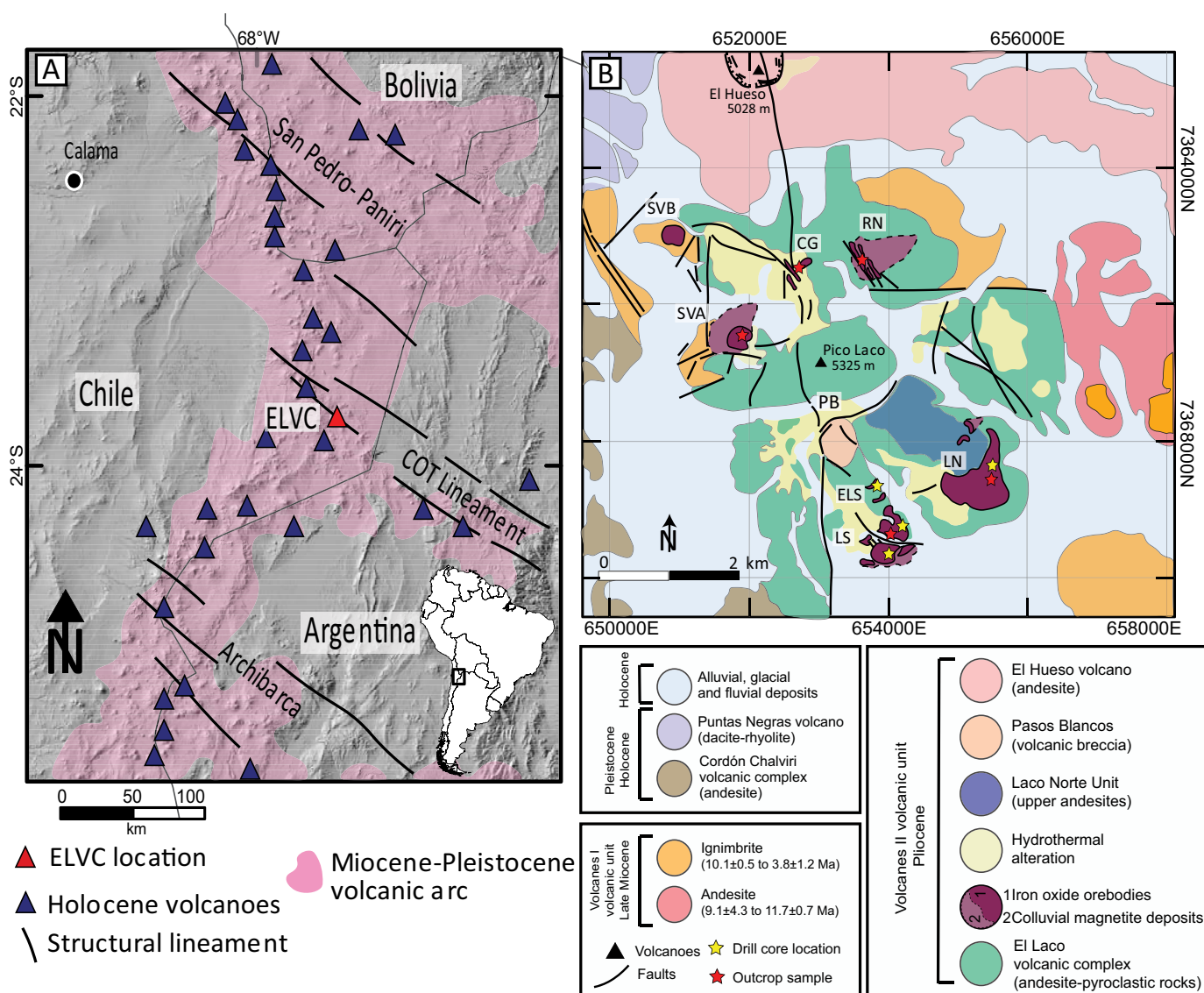


Fig. 1. Maps showing (A) the location of the El Lago Volcanic Complex in the Miocene-Pleistocene volcanic arc on the southwestern coast of South America, and (B) the locations of orebodies and drill core and outcrop samples analyzed in this study. See text for explanation of abbreviations.

Nyström and Henríquez, 1994; Rhodes and Oreskes, 1995; Naslund et al., 2002; Sillitoe and Burrows, 2002; Tornos et al., 2016, 2017; Ovalle et al., 2018). The volcanic host rocks and the orebodies of the El Laco Volcanic Complex have yielded ages ranging from 5.3 ± 1.9 to 1.6 ± 0.5 Ma (K-Ar), and 2.1 ± 0.1 Ma (apatite fission track), respectively (Maksaev et al., 1988; Naranjo et al., 2010). The volcanic rocks in the El Laco Volcanic Complex are andesitic to dacitic in composition with the orebodies distributed around the Pico Laco volcanic edifice (Fig. 1B; Naslund et al., 2002; Tornos et al., 2016; Ovalle et al., 2018). The El Laco ore deposit consists of seven individual orebodies with a total estimated resource endowment of ~734 million tons (Mt) at an average grade of ~49% Fe (CAP Minería, 2014).

Magnetite is the dominant iron oxide in the El Laco deposit, with modal abundances >90 vol %, and apatite, scapolite, and diopside are modally minor phases (Nyström and Henríquez, 1994; Rhodes and Oreskes, 1995, 1999; Rhodes et al., 1999; Naslund et al., 2002; Ovalle et al., 2018). Magnetite is locally altered to hematite and goethite in the upper 40 to 50 m of the orebodies (Ovalle et al., 2018). The orebodies have distinct morphologies and have been classified as (1) flows with feeder dikes (Laco Norte, Laco Sur, San Vicente Alto), (2) dome-like intrusions (San Vicente Bajo), and (3) dikes (Cristales Grandes, Rodados Negros; Nyström and Henríquez, 1994). The massive magnetite orebodies with flow morphology in outcrops contain what appear to be gas escape tubes, and the magnetite contains unfilled vesicles, are coarse grained, and have spherulitic and dendritic textures. Logging of drill cores from Laco Sur and Laco Norte indicate that the outcropping massive magnetite orebodies transition to breccia bodies at depths greater than 40 m (Ovalle et al., 2018). Razor-sharp chilled contacts are observed between the massive magnetite and the host andesite, and friable pyroclastic ore material, including iron oxide ash, is observed near the orebodies (Henríquez and Martin, 1978; Nyström and Henríquez, 1994; Naslund et al., 1997, 1998, 2002; Mungall et al., 2018; Ovalle et al., 2018; Xie et al., 2019).

The host andesite along the margins of the massive magnetite orebodies contains metasomatic aureoles, which are characterized by an alteration assemblage containing pyroxene, magnetite, quartz, and scapolite (Vivallo et al., 1994; Naslund et al., 2002; Velasco et al., 2016). The alteration assemblages observed in the host rocks below the flow-like orebodies include clays (illite, smectite), pyrophyllite, quartz, feldspar, and magnetite veinlets without pyroxene fringes (Broman et al., 1999; Naslund et al., 2002). Minerals including quartz, tridymite, amorphous silica, hematite, Na-rich alunite, iron phosphates, labradorite, sanidine, and rutile are observed in vesicles in the extrusive orebodies (Naslund et al., 2002). The host rocks are also overprinted by postmineralization low-temperature hydrothermal alteration that is manifested as silicification (characterized by quartz, tridymite, cristobalite, alunite, jarosite, K-feldspar, anatase, iron phosphates, iron sulfates), advanced argillic alteration (characterized by quartz, alunite, kaolinite, gypsum, cristobalite, smectite, bassanite, pyrite, pyrophyllite), and the formation of fumarolic deposits (characterized by gypsum, alunite, jarosite, native sulfur, cristobalite, tridymite,

calcite) (Vivallo et al., 1994; Broman et al., 1999; Naslund et al., 2002; Sillitoe and Burrows, 2002).

Sample Selection and Methodology

Magnetite-rich ore samples from outcrops at the Cristales Grandes (CG), Rodados Negros (RN), San Vicente Alto (SVA), Laco Norte (LN), and Laco Sur (LS) orebodies, and drill core samples at Laco Norte, Laco Sur, and Extensión Laco Sur (Fig. 1B) were collected. We analyzed magnetite grains from outcrop and representative drill core samples, and apatite grains collected from outcrops at Cristales Grandes, Rodados Negros, and Laco Sur. Apatite was scarcely observed in drill core samples and was not analyzed as part of the current study; apatite from drill core samples will be the focus of a future study. Outcrop magnetite samples were examined by using an optical microscope and then crushed and separated into two aliquots: one aliquot was used in this study, and the second in a separate study that measured Fe, H, and O stable isotope concentrations (Childress et al., 2020). For this study, a combination of thin and thick sections and grain mounts were prepared for detailed petrographic inspection and microtextural observations of magnetite and apatite grains.

Imaging and electron probe microanalyses

Magnetite: Magnetite grains from outcrop samples at the five orebodies (Cristales Grandes, Rodados Negros, San Vicente Alto, Laco Norte, Laco Sur) were characterized by backscattered electron (BSE) imaging and energy-dispersive X-ray spectrometry (EDS) elemental mapping by using the JEOL JSM-7800FLV field-emission scanning electron microscope (FE-SEM) at the University of Michigan Electron Microbeam Analysis Laboratory, using an accelerating voltage of 15 kV and a medium beam current. Drill core samples were characterized by using a Model FEI Quanta 250 SEM at Universidad de Chile with an accelerating voltage of 12.5 kV. Quantitative compositional analyses of all magnetite grains were performed by using the University of Michigan Electron Microbeam Analysis Laboratory Cameca SX100 electron probe microanalyzer (EPMA) in wavelength-dispersive X-ray spectrometry (WDS) mode. The concentrations of Fe, Ti, V, Mn, Ca, P, Mg, Cr, Al, and Si were measured by using an accelerating voltage of 20 keV, a beam current of 30 nA, and a focused electron beam. The counting times and standards used are presented in Table A1. Vanadium measurements were corrected for the spectral overlap of the V K α X-ray line by the Ti K β . A total of 1,917 individual EPMA spot analyses were conducted on representative iron oxide grains from the outcrop and drill core samples collected at the five orebodies. These EPMA data are presented in the electronic supplementary materials of Ovalle et al. (2018).

Apatite: The apatite grains from the three orebodies (Cristales Grandes, Rodados Negros, Laco Sur) were investigated by using a combination of BSE and cathodoluminescence (CL) imaging, and EDS element mapping, by using an accelerating voltage of 20 kV on the University of Michigan Electron Microbeam Analysis Laboratory FE-SEM. Quantitative compositional analyses were made by using the University of Michigan Electron Microbeam Analysis Laboratory EPMA and the Cameca SX100 EPMA at the American Museum of Natural History in New York. Line transects and spot analyses

were performed on apatite grains in thin section (Laco Sur) and epoxy mounts (Cristales Grandes and Rodados Negros), and the measurements were made by using an excitation voltage of 15 keV, a beam current of 10 nA, and a spot size of 2 to 10 μm . The standards, counting times, and analytical conditions are presented in Table A2. Calcium, P, Cl, and F were analyzed first in the analytical sequence as suggested by Goldoff et al. (2012) to mitigate elemental migration during the analyses. The hydroxide (OH) content of apatite for individual spot analyses was calculated using the mass balance method of Ketcham (2015), which uses the measured Cl and F concentrations and the assumption that the halogen site in apatite is occupied by $X_F + X_{Cl} + X_{OH} = 1$.

LA-ICP-MS analyses

Laser ablation inductively coupled plasma mass spectrometry (LA-ICP-MS) analyses of magnetite and apatite were performed by using a Thermo Scientific iCapQ quadrupole inductively coupled plasma mass spectrometer (ICP-MS), coupled with a 193-nm ArF excimer laser at the Andean Geothermal Center of Excellence laboratory at Universidad de Chile. The LA-ICP-MS analyses were performed along the same transects that were previously analyzed by EPMA in order to obtain trace element chemistry to complement the major and minor element chemistry obtained via EPMA. The concentrations of the elements analyzed, and their associated limits of detection were determined by using the Iolite software package (Paton et al., 2011) based on Longerich et al. (1996). Each LA-ICP-MS transient signal was evaluated for the presence of inclusions, and only inclusion-free signals were considered.

Magnetite: The concentrations of Na, Mg, Al, Si, P, S, K, Ca, Sc, Ti, V, Cr, Mn, Co, Ni, Cu, Zn, Ga, Ge, As, Se, Kr, Rb, Sr, Y, Zr, Nb, Mo, Ag, Cd, Sn, Sb, Te, Ba, Hf, Ta, Au, Pb, Th, U, and rare earth elements (REEs; La, Ce, Pr, Nd, Sm, Eu, Gd, Tb, Dy, Ho, Er, Tm, Yb, Lu) were measured in magnetite from outcrop and drill core samples from the five orebodies. Additionally, tungsten was measured in magnetite grains from the drill core samples. A beam diameter of 40 μm was used to conduct spot analyses. The iron concentrations previously quantified by using EPMA were used as the internal standard for LA-ICP-MS calibration, and the analyses of the samples were bracketed at the start and end of each run by pairs of analyses of the GSE-1G (Jochum et al., 2005) reference glass. A pair of analyses on the NIST-610 or GSE-1D reference glasses were done prior to the spot analyses, and after the initial pair of analyses of the GSE-1G reference glass, to evaluate the accuracy of the analyses (Jochum et al., 2005, 2011). Details of the analytical protocol are presented in Appendix 1.

Apatite: The concentrations of Na, Mg, Al, Si, P, S, Cl, Sc, Ti, V, Cr, Mn, Fe, Co, Ni, Cu, Zn, Ge, As, Rb, Sr, Y, Zr, Nb, Mo, Xe, Ba, Hf, Ta, W, Os, Pb, Th, U, and REEs (La, Ce, Pr, Nd, Sm, Eu, Gd, Tb, Dy, Ho, Er, Tm, Yb, Lu) were measured in apatite from Cristales Grandes and Rodados Negros. No LA-ICP-MS analyses were performed on apatite from Laco Sur because the grains were too small to analyze. A beam diameter of 30 μm was utilized for the analyses. Calcium concentrations previously quantified by using EPMA were used as the internal standard for LA-ICP-MS calibration. The NIST-610 reference glass was used as the bracketing external calibration standard, and the Durango apatite (Chew et al., 2016) was measured

twice prior to the analysis of the samples and after the initial analyses of the NIST-610 (Jochum et al., 2011) glass during each run to evaluate the accuracy of the analyses. Details of the analytical conditions are presented in Appendix 1

Results

Magnetite textures and associated minerals

Backscattered electron imaging of surface samples revealed the presence of magnetite with differing minor and trace element compositions and the presence of martite/hematite and goethite in some samples (Fig. 2). Magnetite expresses itself in at least seven variations, based on BSE imagery, texture, paragenesis, and composition (Table 1, Fig. 2). Light-gray magnetite in the BSE images of samples from Cristales Grandes (magnetite S1) contains nanoinclusions, whereas nanoinclusions were not observed in light-gray magnetite (magnetite S2) from other orebodies (Fig. 2B-H). In BSE images from all orebodies, we observe magnetite A, which is a darker shade of gray compared to magnetite S1 and S2 (Fig. 2F, H). Hematite was observed in samples from Cristales Grandes, San Vicente Alto, Laco Sur, and Laco Norte (Fig. 2A, C, G), but not in samples from Rodados Negros. Goethite was identified in surface samples from all orebodies except Cristales Grandes and Rodados Negros (Fig. 2C, G, H). Magnetite grains in surface samples from all orebodies commonly meet at triple junctions and contain mineral inclusions (Fig. 2H). Apatite occurs as inclusions and/or within fractures in magnetite from Cristales Grandes, Rodados Negros, Laco Sur, and Laco Norte (Fig. 2D). Pyroxene is present as intergrowths in magnetite grains from Cristales Grandes, Rodados Negros, and San Vicente Alto (Fig. 2A). Monazite is present as inclusions and/or within fractures in magnetite grains from San Vicente Alto, Laco Norte, and Laco Sur (Fig. 2B, D). Quartz and an iron phosphate phase, which appear to be the alteration product of apatite, are present as inclusions in some magnetite grains from San Vicente Alto and Laco Norte (Fig. 2B). Thorite is present as inclusions in some magnetite grains from Laco Norte (Fig. 2C). An Nb-rich oxide phase with a composition similar to columbite is present as inclusions within one magnetite sample from Laco Sur (Fig. 2F). Magnetite in surface samples contain visible microporosity.

Textures observed by BSE imaging of samples from drill core at Laco Norte and Laco Sur are described in detail by Ovalle et al. (2018) and shown here in Figure 2. In ore samples from the deepest zones (>152 m) at Laco Sur, Extensión Laco Sur, and Laco Norte, we observe agglomerates of titanomagnetite grains that range in size from 100 to 300 μm and contain well-developed trellis- and sandwich-textured ilmenite oxyexsolution lamellae (magnetite- α ; Fig. 2I), and euhedral magnetite grains with inclusion-rich cores, surrounded by inclusion-free rims (magnetite- β ; Fig. 2M). Magnetite grains from the deepest samples at Laco Sur contain more ilmenite oxyexsolution lamellae than samples from Laco Norte (Fig. 2P). In samples from intermediate depths (66–144 m), we observe magnetite grains up to 500 μm in size that each have an inclusion-free microcrystalline core (magnetite-X) surrounded by alternating layers of inclusion-rich and -poor magnetite (magnetite-Y; Fig. 2J). In the upper 65 m of the deposit, we observe agglomerates of euhedral magnetite grains (magnetite-Z) that are weakly to

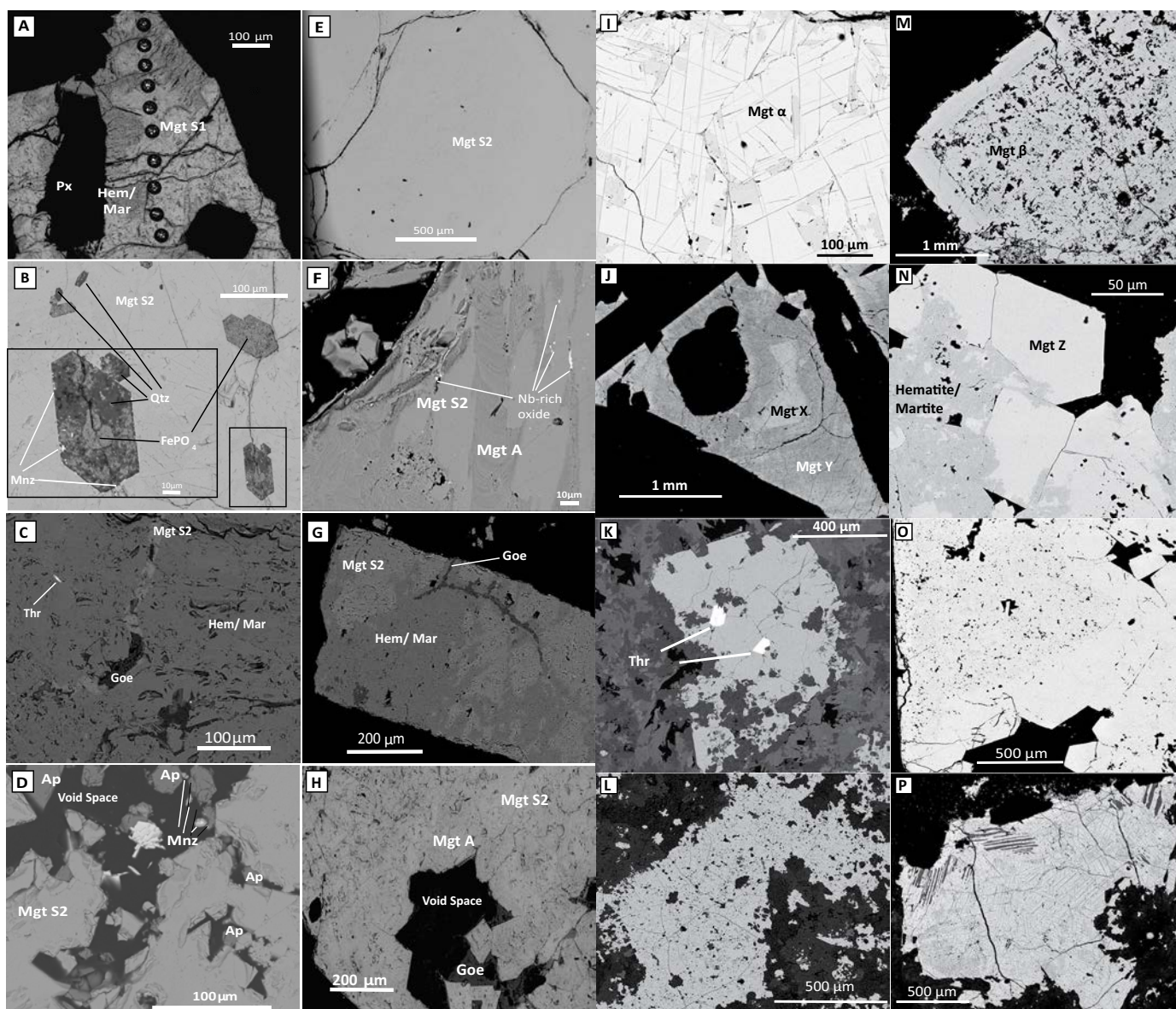
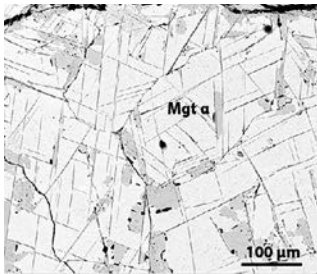
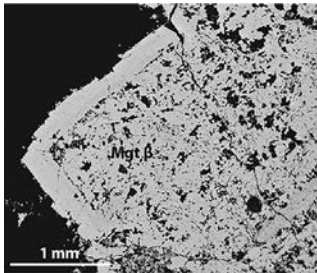
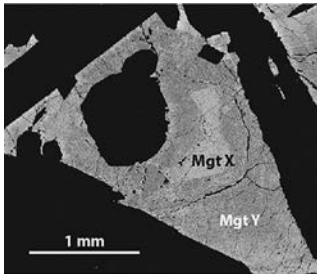
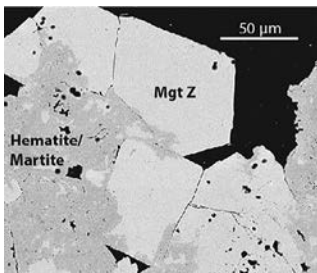
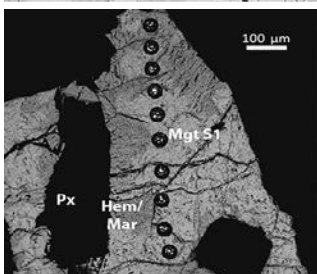
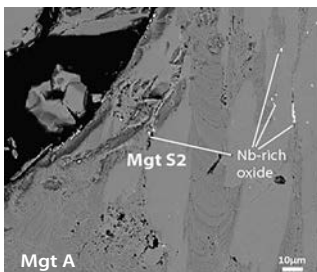


Fig. 2. Representative backscattered electron (BSE) images of surface and drill core samples from orebodies at El Laco. Dark/black areas in all images are void space. (A). Sample from Cristales Grandes containing magnetite (Mgt S1), which is altered to hematite (Hem)/martite (mar), and pyroxene (px; composition similar to diopside and augite). Craters from the LA-ICP-MS transect are visible in the image. (B). Sample from San Vicente Alto, showing magnetite (Mgt S2) with euhedral hexagonal iron phosphate (FePO_4) intergrowths, which are paragenetically early and formed pre- or synmagnetite. The FePO_4 intergrowths also contain monazite (Mnz) grains interspersed within them, and at grain boundaries formed with magnetite. Finally, some FePO_4 grains contain quartz (Qtz), which is paragenetically later than the FePO_4 (because the FePO_4 is enveloped by the quartz, as highlighted in the inset). (C). Sample from Laco Norte containing magnetite, hematite, goethite (Goe), and thorite inclusions (Thr). (D). Sample from Laco Sur containing apatite (Ap) and monazite inclusions. (E). Massive magnetite grains from Rodados Negros that are subhedral and inclusion free. (F). Sample from Laco Sur containing magnetite, patches of magnetite with high Si and Mg content (Mgt A), and Nb-rich oxide inclusions in cracks and at the boundary of the two generations of magnetite. (G). Sample from Laco Sur containing magnetite, hematite, and goethite (Goe). (H). Sample from Laco Norte containing magnetite-A and magnetite-S2, and goethite (Goe). (I). Sample from deep zone of Laco Norte, showing an aggregate of titanomagnetite crystals (Mgt- α) displaying trellis-textured ilmenite exsolution lamellae. (J). Sample from intermediate zone of Laco Norte, showing a partially dissolved magnetite (Mgt-X) core, which is overgrown by a later magnetite (Mgt-Y) defined by the presence of oscillatory textures of inclusion-rich and -poor alternating growth zones. (K-L). Samples from intermediate zones of Laco Sur that correspond to a magnetite-scapolite-pyroxene-rich zone. Thorite inclusions are common in this zone (K). (M). Sample from the deep zone of Laco Norte, showing a euhedral core of inclusion-rich magnetite- β surrounded by a rim of inclusion-poor magnetite. (N). Sample from the shallow zone of Laco Norte containing an aggregate of inclusion-poor magnetite-Z grains, partially oxidized to martite/hematite. (O). Sample from shallow depths of Laco Sur, showing a coarse magnetite grain containing an inclusion-rich core surrounded by a rim of inclusion-poor magnetite. (P). Sample from the deep zone of Laco Sur displaying titanomagnetite (Mgt- α) grains from the breccia matrix, which contain well-developed ilmenite exsolution lamellae that exhibit both trellis and sandwich textures.

Table 1. Summary of the Characteristics of the Eight Different Types of Magnetite Observed at El Laco

Magnetite (name/generation)	Characteristics	Color in BSE images	Depth	Representative BSE Image
Magnetite- α	Contains trellis and sandwich-textured ilmenite exsolution lamellae	Light gray	Deep drill core (>150 m)	
Magnetite- β	Inclusion-rich cores surrounded by inclusion-poor rims	Gray	Deep drill core (150 m)	
Magnetite-X	Inclusion-free microcrystalline core	Gray	Intermediate depths in drill core (65–145 m)	
Magnetite-Y	Bands of inclusion-rich and -poor magnetite	Dark gray	Intermediate depths (65–145 m)	
Magnetite-Z	Euhedral magnetite agglomerates that are weakly to moderately oxidized to hematite	Gray	Shallow depths (<65 m)	
Magnetite S1	Has nanoinclusions	Light gray	Surface outcrop	
Magnetite S2	No nanoinclusions	Light gray	Surface outcrop	
Magnetite A	Higher Si contents	Dark gray	Surface outcrop	

moderately oxidized to hematite/martite along rims and in fractures (Fig. 2N). Magnetite grains from the upper 65 m of drill core also contain visibly abundant microporosity. Magnetite in surface samples from Laco Sur and Laco Norte are replaced by hematite and minor goethite, whereas samples at depth show little or no alteration. Rare scapolite inclusions are observed in magnetite from the deep zones at Laco Sur and Laco Norte. Inclusions of thorite are observed in magnetite at intermediate depths at Laco Sur and Laco Norte (Fig. 2K), and inclusions of clinopyroxene, with compositions similar to diopside and augite, are observed in magnetite at all depths in the drill cores from Laco Sur and Laco Norte.

Magnetite chemistry

Major, minor, and trace element compositions for magnetite from all samples are presented in Table A3 and average, minimum, and maximum values in Table 2. The concentrations of Au, Ag, Cu, As, Rb, Cd, Sb, Pb, W, Se, Kr, Te, and S were below the limit of detection for many analyses. The light-gray magnetite (magnetite S1 and S2) observed in BSE images of outcrop samples from all orebodies has average measured Fe concentrations ranging from 69 to 71 wt %, and notably has higher concentrations of minor and trace elements compared to hematite and goethite. The gray magnetite phase (magnetite A) in samples from Cristales Grandes, Rodados Negros, and Laco Sur has average measured Fe concentrations ranging from 69.0 to 69.5 wt %, and generally has higher silica content than magnetite S1 or S2. The average major and minor element compositions for magnetite from the drill core and surface samples at Laco Sur and Laco Norte were previously reported by Ovalle et al. (2018). The measured concentrations of minor and trace elements in magnetite from outcrops and drill cores are presented in Table 2, and Ti, V, Al, Mn, Sn, and Ga concentrations are plotted in Figure 3. The concentrations of Ti, V, Al, Mn, Ga, and Sn decrease progressively in magnetite from Cristales Grandes to Rodados Negros to San Vicente Alto, whereas the concentration of Ni increases (Fig. 3, Fig. A1). The concentrations of Ni, Ti, V, Mn, Co, Ga, and Al in magnetite from Laco Norte generally increase with increasing depth in the deposit, whereas the concentration of Sn is almost constant in drill core samples but markedly higher in surface samples. At Laco Sur, the concentrations of Ti, Zn, Al, Cr, Ga, Ni, and V increase from surface to depth.

In Figures 4, 5, and A2, we present comparisons of the average concentrations of minor and trace elements normalized to bulk continental crust (cf. Rudnick and Gao, 2003) for magnetite sampled from outcrop and drill core along with compositional data from Dare et al. (2014) for magnetite from Kiruna-type deposits, including El Laco, magmatic (i.e., intermediate to felsic igneous rocks), magmatic-hydrothermal (i.e., porphyry), and low-temperature hydrothermal (i.e., banded iron formations and skarns) environments. Magnetite from magmatic, magmatic-hydrothermal, and low-temperature hydrothermal environments crystallizes from fluids at temperatures >500°, between 300° to 500°, and between 200° to 300°C, respectively (Nadoll et al., 2014). The compositions of magnetite from outcrop and drill core samples overlap the fields for magnetite from igneous rocks, magmatic-hydrothermal environments, and Kiruna-type ore deposits. There is minimal overlap between the El Laco samples and

low-temperature hydrothermal magnetite. We highlight that the titanium concentrations of magnetite grains that contain ilmenite oxyexsolution lamellae (Fig. 2I, P) are lower than the original titanium content of magnetite owing to the partitioning of titanium into oxyexsolved ilmenite lamellae.

In Figure 6, the concentrations of [Al + Mn] and [Ti + V] in magnetite from the surface (A) and drill core (B) samples are plotted in the magnetite discriminant diagram of Nadoll et al. (2014). Also plotted in Figure 6 are the [Al + Mn] and [Ti + V] concentrations of magnetite from the El Laco andesite host (cf. Dare et al., 2015). Colored contours represent the temperatures of crystallization of magnetite reported by Nadoll et al. (2014). The concentrations of Al, Mn, Ti, and V are highest in magnetite from the host andesite and decrease progressively among the surface samples from Cristales Grandes to Rodados Negros to San Vicente Alto (Fig. 6A). The [Ti + V] content of magnetite from the deepest drill core samples from Laco Sur is similar to igneous magnetite from iron-titanium-vanadium (Fe-Ti,V) deposits and trends toward the composition of magnetite from the El Laco andesite host, although the drill core samples have lower [Al + Mn] contents (Fig. 6B). For all magnetite samples from the drill core, [Al + Mn] and [Ti + V] contents decrease from depth to surface (Fig. 6D).

Apatite textures and associated minerals

The apatite grains from Cristales Grandes, Rodados Negros, and Laco Sur are almost homogeneous in color in BSE images, except for a few grains from Cristales Grandes, which exhibit growth zones of lighter color (Fig. 7A, C, E). Generally, the apatite in samples from all three orebodies contains varying amounts of microporosity, fractures, and inclusions (Fig. 7A, C, E). The EDS element maps of the apatite grains indicate homogeneous distribution of Ca and P. The EDS maps indicate a heterogeneous distribution of sulfur in apatite from Laco Sur where the concentrations of sulfur are higher near grain boundaries and proximal to cracks within grains (Fig. 7G). Variations in cathodoluminescence intensity were observed in apatite grains from all samples. At Cristales Grandes, most of the apatite grains display purple luminescence, while the areas with lighter color in BSE display dark blue luminescence; oscillatory growth zoning is observed in CL images in some grains from this orebody (Fig. 7B). Apatite grains from Rodados Negros display mauve luminescence, while the highly porous regions of the grains display orange luminescence (Fig. 7D). The apatite from Laco Sur displays purple or blue luminescence in the inner portions of the grains, whereas the grain boundaries and areas proximal to cracks, which have higher S contents, display dark or minimal luminescence (Fig. 7F). Growth zoning is not observed in the apatite grains from Rodados Negros and Laco Sur. Monazite is present as inclusions and in cracks and on grain boundaries in apatite grains from Cristales Grandes and Rodados Negros; these inclusions are more common in the mottled/porous regions of apatite grains from Rodados Negros (Fig. 7A, C). Small euhedral magnetite grains are observed within agglomerates of apatite from Laco Sur (Fig. 7E).

Apatite chemistry

The major, minor, and trace element compositions for apatite from all samples are presented in Appendix Spreadsheet

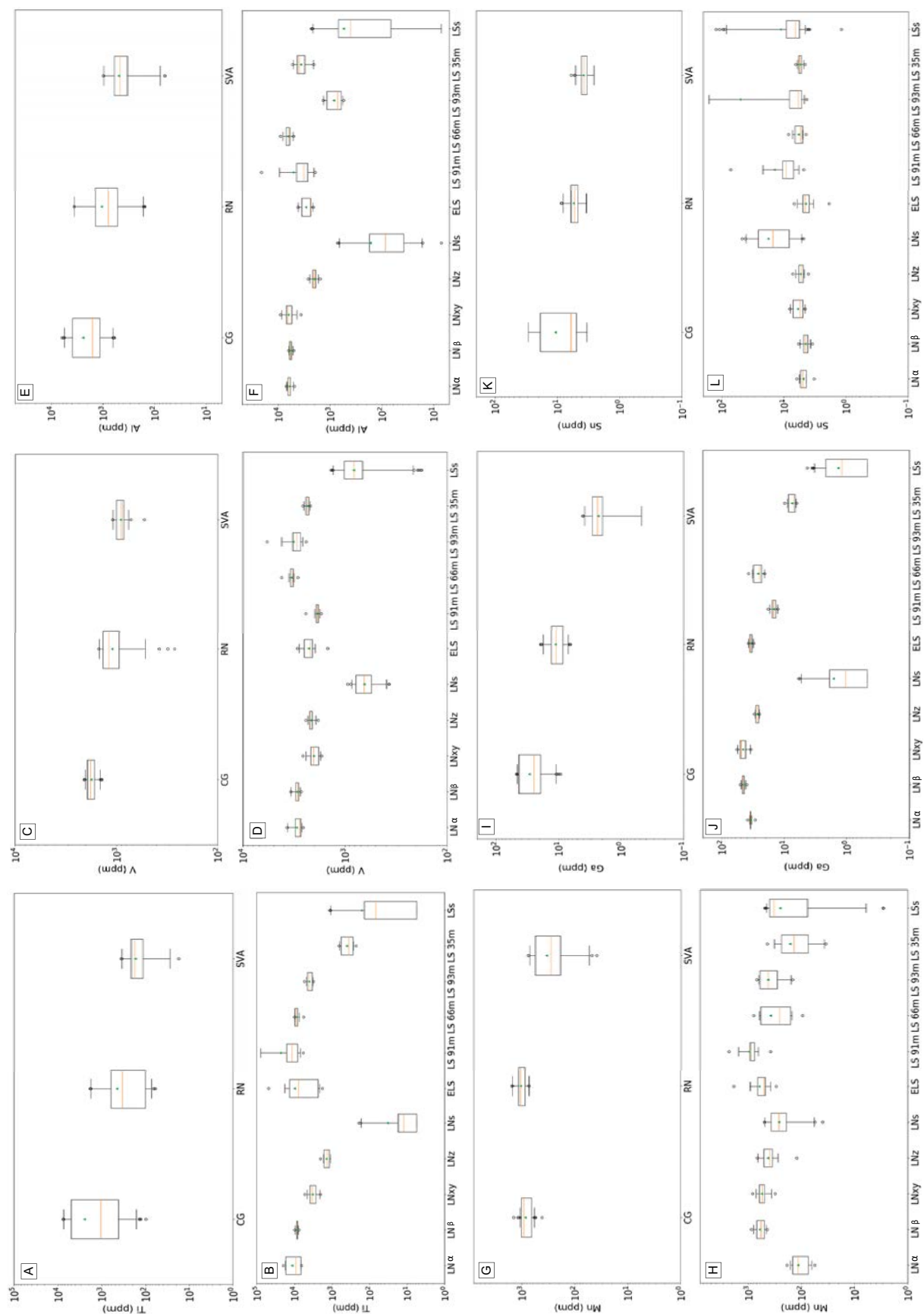


Fig. 3. Minor and trace element geochemistry of magnetite from surface samples from the Cristales Grandes (CG), Rodados Negros (RN), and San Vicente Alto (SVA) orebodies from the El Laco deposit (A, C, E, G, I). Data for magnetite from surface outcrops and drill core samples from the Laco Norte (LN), Extensión Laco Sur (ELS), and Laco Sur (LS) orebodies are displayed in B, D, F, H, J. Textural varieties of magnetite from LN are denoted by the same symbols as in Figure 2 (α , β , X, Y, Z, S). Additionally, the depths from which drill core samples from LS were collected are indicated, e.g., LS 91 m. The orange line in each box represents the median concentration, and the green triangles represent the mean values. The upper and lower margins of the box identify the upper and lower 50% of the data, while the whiskers show the range of concentrations for 95% of the data.

Table 2. Summary of Compositions of Magnetite from Outcrops at Cristales Grandes, Rodados Negros, San Vicente Alto, and Outcrops and Drill Core at Laco Norte

Laco Norte: Surface/outcrop									
		Magnetite S2 N = 14				Magnetite A N = 15			
	D.L.	Min.	Mean	Max.	Std. dev	Min.	Mean	Max.	Std. dev
EPMA									
Fe (wt %)	0.02	67.30	69.55	70.98	1.16	64.73	66.88	69.35	1.52
Ti (ppm)	89.46	B.D.L.	B.D.L.	170.00	42.66	B.D.L.	101.61	212.00	58.55
V (ppm)	66.39	359.00	817.57	1,208.00	359.81	401.00	532.80	629.00	74.39
Al (ppm)	81.24	115.00	3,923.64	39,767.00	10,549.22	85.00	1,108.47	7,764.00	1,870.72
Mn (ppm)	80.45	B.D.L.	152.72	387.00	110.25	B.D.L.	290.66	504.00	185.19
Mg (ppm)	128.04	2,618.00	8,795.86	15,627.00	3,233.57	5,956.00	13,375.47	20,437.00	4,745.11
Si (ppm)	68.07	454.00	3,642.29	10,293.00	3122.77	318.00	11,239.27	18,839.00	7,011.18
P (ppm)	83.51	B.D.L.	110.81	559.00	153.97	B.D.L.	177.47	960.00	227.30
Ca (ppm)	83.73	124.00	1,262.29	3,261.00	1,100.96	B.D.L.	3,421.12	5,509.00	2,036.13
Cr (ppm)	62.61	B.D.L.	B.D.L.	151.00	31.99	B.D.L.	B.D.L.	B.D.L.	0.00
LA-ICP-MS (ppm)									
Na	56.67	60.00	463.14	856.00	275.85	76.00	832.93	1205.00	385.76
Mg	43.53	503.00	8,311.64	11,320.00	2,744.30	6,480.00	11,180.00	14,800.00	3,017.02
Al	36.52	B.D.L.	39.12	110.00	34.36	B.D.L.	377.25	717.00	309.58
Si	2,989.50	B.D.L.	7,163.91	11,500.00	3,424.70	B.D.L.	15,966.32	33,900.00	10,620.55
P	9.57	43.00	157.07	371.00	96.54	B.D.L.	187.25	343.00	79.60
K	35.84	B.D.L.	150.57	252.00	80.46	65.00	360.40	594.00	181.36
Ca	738.79	B.D.L.	1,763.36	3,830.00	1,323.37	B.D.L.	3231.92	6,500.00	2,005.61
Sc	4.90	B.D.L.	B.D.L.	B.D.L.	0.00	B.D.L.	3.12	8.70	1.82
Ti	37.26	B.D.L.	B.D.L.	B.D.L.	0.00	B.D.L.	91.23	191.00	83.25
V	14.33	370.00	638.36	842.00	157.40	404.00	521.53	606.00	66.08
Cr	3.40	B.D.L.	B.D.L.	B.D.L.	0.00	B.D.L.	B.D.L.	3.80	0.54
Mn	5.59	57.10	247.92	374.00	134.16	55.30	305.33	496.00	183.88
Co	2.13	60.50	115.23	153.00	22.39	106.00	128.68	168.00	21.07
Ni	4.44	175.00	227.03	253.00	22.59	188.00	212.60	246.00	17.22
Cu	1.76	B.D.L.	6.21	34.30	10.65	B.D.L.	6.36	29.20	9.95
Zn	5.57	15.60	39.54	56.90	14.24	20.20	55.26	118.00	22.41
Ga	0.94	B.D.L.	B.D.L.	1.54	0.37	B.D.L.	3.14	5.90	2.40
Ge	2.19	21.50	24.35	26.20	1.61	21.50	24.05	27.80	1.80
As	5.51	B.D.L.	22.25	33.40	11.46	B.D.L.	20.37	35.00	9.62
Rb	1.09	B.D.L.	B.D.L.	2.40	0.50	B.D.L.	B.D.L.	1.56	0.34
Sr	0.08	0.79	5.45	13.40	2.94	0.90	6.48	9.70	2.83
Y	0.99	1.68	14.80	24.50	7.25	1.74	30.03	57.60	19.27
Zr	0.08	B.D.L.	0.18	0.64	0.18	B.D.L.	1.76	3.70	1.52
Nb	0.27	1.00	31.23	63.30	22.29	1.25	38.37	74.00	28.00
Mo	1.42	B.D.L.	B.D.L.	3.40	0.86	B.D.L.	1.67	7.50	1.93
Ag	1.73	B.D.L.	B.D.L.	B.D.L.	0.00	B.D.L.	B.D.L.	B.D.L.	0.00
Cd	0.36	B.D.L.	0.48	2.00	0.44	B.D.L.	B.D.L.	B.D.L.	0.00
Sn	0.95	6.20	11.53	15.92	3.65	5.72	14.64	24.30	6.85
Sb	1.28	B.D.L.	2.83	5.11	1.79	B.D.L.	3.34	6.80	2.43
Ba	0.15	0.44	4.14	6.53	1.80	0.73	3.50	6.90	2.41
La	0.21	3.38	31.70	58.20	16.68	1.78	7.23	11.40	2.67
Ce	0.46	12.80	77.81	133.70	37.72	3.26	53.28	86.10	28.73
Pr	0.07	1.02	8.22	14.87	4.31	9.48	119.87	193.00	62.12
Nd	0.27	3.60	29.33	53.50	14.61	0.85	12.81	20.50	6.66
Sm	0.25	B.D.L.	4.27	7.70	2.33	2.66	44.20	80.80	25.04
Eu	0.05	B.D.L.	0.54	0.97	0.29	0.67	6.50	11.50	3.59
Gd	0.18	B.D.L.	3.56	7.40	1.97	B.D.L.	0.69	1.33	0.39
Tb	0.06	B.D.L.	0.44	0.75	0.23	B.D.L.	0.87	1.59	0.51
Dy	0.20	B.D.L.	2.97	4.88	1.53	0.25	5.27	9.80	3.54
Ho	0.08	B.D.L.	0.54	0.87	0.29	B.D.L.	1.16	2.40	0.77
Er	0.15	B.D.L.	1.63	3.00	0.90	0.08	3.67	7.60	2.64
Tm	0.09	B.D.L.	0.25	0.41	0.13	B.D.L.	0.60	1.29	0.49
Yb	0.19	B.D.L.	B.D.L.	2.81	0.89	B.D.L.	4.72	8.80	3.45
Lu	0.08	B.D.L.	0.32	0.52	0.17	B.D.L.	0.76	1.61	0.63
Hf	0.07	B.D.L.	B.D.L.	B.D.L.	0.00	B.D.L.	B.D.L.	0.04	0.00
Ta	0.07		0.19	0.37	0.10	B.D.L.	1.46	2.88	1.17
W	0.49	N.M.	N.M.	N.M.	N.M.	N.M.	N.M.	N.M.	N.M.
Au	0.03	B.D.L.	B.D.L.	B.D.L.	0.00	B.D.L.	B.D.L.	B.D.L.	0.00
Pb	0.44	B.D.L.	B.D.L.	B.D.L.	0.00	B.D.L.	B.D.L.	B.D.L.	0.00
Th	0.31	3.83	40.52	65.10	20.80	3.08	89.72	157.00	56.72
U	0.11	0.37	4.03	6.67	2.11	0.68	7.46	14.30	5.28

Table 2. (Cont.)

Laco Norte: Deep drill core									
	D.L.	Magnetite α N = 9				Magnetite β N = 20			
		Min.	Mean	Max.	Std. Dev	Min.	Mean	Max.	Std. Dev
EPMA									
Fe (wt %)	0.02	68.72	69.96	71.18	0.84	67.91	69.50	70.41	0.77
Ti (ppm)	89.46	3,826.61	8,389.02	16,586.21	4,205.36	755.45	5,860.43	15,432.87	3,012.86
V (ppm)	66.39	1,170.52	1,330.50	1,589.70	151.37	1,059.68	1,288.89	1,439.84	75.62
Al (ppm)	81.24	4,870.00	6,127.78	6,960.00	728.11	1,315.25	2,111.78	2,921.76	393.52
Mn (ppm)	80.45	B.D.L.	B.D.L.	274.64	91.55	B.D.L.	294.25	967.80	282.76
Mg (ppm)	128.04	712.78	2,484.46	4,351.13	1,071.58	1,636.74	5,997.97	9,638.92	1,939.45
Si (ppm)	68.07	100.67	130.25	184.40	25.20	111.49	760.12	6,052.66	1,422.92
P (ppm)	83.51	B.D.L.	B.D.L.	B.D.L.	B.D.L.	B.D.L.	B.D.L.	B.D.L.	0.00
Ca (ppm)	83.73	B.D.L.	B.D.L.	124.90	41.63	B.D.L.	679.10	4258.66	1255.68
Cr (ppm)	62.61	B.D.L.	B.D.L.	B.D.L.	0.00	B.D.L.	B.D.L.	B.D.L.	0.00
LA-ICP-MS (ppm)	D.L. (ppm)								
Na	56.67	B.D.L.	B.D.L.	103.00	27.88	B.D.L.	448.65	4,310.00	930.72
Mg	43.53	881.00	2,534.33	4,490.00	1,110.76	5,610.00	8,124.50	10,130.00	1,363.01
Al	36.52	4,870.00	6,127.78	6,960.00	728.11	5,086.00	5,863.80	6,350.00	379.85
Si	2,989.50	B.D.L.	B.D.L.	9,100.00	2,383.40	B.D.L.	3,522.83	9,900.00	2,119.59
P	9.57	10.16	29.74	117.00	35.60	10.16	41.98	107.00	32.06
K	35.84	B.D.L.	B.D.L.	45.00	17.65	B.D.L.	130.36	351.00	117.26
Ca	738.79	B.D.L.	794.15	3,700.00	1,098.80	B.D.L.	B.D.L.	1,880.00	485.98
Sc	4.90	B.D.L.	5.29	11.10	2.47	B.D.L.	7.30	11.60	2.55
Ti	37.26	6,540.00	11,537.78	20,200.00	5,365.23	7,680.00	8,654.00	9,870.00	547.66
V	14.33	2,580.00	2,978.00	3,690.00	423.21	2,690.00	2,957.40	3,400.00	207.25
Cr	3.40	B.D.L.	8.13	42.70	13.07	B.D.L.	4.69	10.00	2.60
Mn	5.59	55.60	115.31	186.00	46.41	441.00	606.75	872.00	130.72
Co	2.13	141.20	159.74	174.40	11.10	120.80	148.88	171.30	13.68
Ni	4.44	402.00	440.00	476.00	29.64	344.00	391.67	428.00	24.13
Cu	1.76	B.D.L.	1.93	9.40	2.82	B.D.L.	B.D.L.	2.68	0.66
Zn	5.57	64.20	74.14	90.60	11.21	65.40	93.64	127.00	14.43
Ga	0.94	29.20	34.51	38.50	2.47	39.70	45.51	50.50	2.66
Ge	2.19	2.30	3.00	4.30	0.64	B.D.L.	2.36	3.11	0.51
As	5.51	B.D.L.	B.D.L.	B.D.L.	0.00	B.D.L.	B.D.L.	11.40	2.63
Rb	1.09	B.D.L.	B.D.L.	B.D.L.	0.00	B.D.L.	B.D.L.	2.83	0.79
Sr	0.08	B.D.L.	0.46	4.10	1.37	0.00	1.57	8.40	2.31
Y	0.99	B.D.L.	B.D.L.	4.41	1.41	B.D.L.	1.07	4.47	1.21
Zr	0.08	B.D.L.	2.64	6.80	1.87	0.90	4.53	12.20	3.48
Nb	0.27	B.D.L.	0.54	1.29	0.41	B.D.L.	0.68	1.97	0.52
Mo	1.42	B.D.L.	1.47	2.00	0.20	1.40	1.41	1.51	0.02
Ag	1.73	B.D.L.	B.D.L.	B.D.L.	0.00	B.D.L.	B.D.L.	B.D.L.	0.00
Cd	0.36	B.D.L.	B.D.L.	B.D.L.	0.00	B.D.L.	B.D.L.	B.D.L.	1.00
Sn	0.95	3.26	4.93	6.28	0.87	3.49	4.56	5.80	0.60
Sb	1.28	B.D.L.	B.D.L.	B.D.L.	0.00	B.D.L.	B.D.L.	1.37	0.35
Ba	0.15	B.D.L.	B.D.L.	0.36	0.12	B.D.L.	2.97	36.00	7.89
La	0.21	B.D.L.	B.D.L.	0.94	0.31	B.D.L.	1.07	3.67	1.18
Ce	0.46	B.D.L.	B.D.L.	2.31	0.76	B.D.L.	2.62	10.23	3.05
Pr	0.07	B.D.L.	B.D.L.	0.38	0.13	B.D.L.	0.36	1.88	0.51
Nd	0.27	B.D.L.	B.D.L.	1.08	0.36	B.D.L.	1.50	7.20	2.08
Sm	0.25	B.D.L.	B.D.L.	0.94	0.31	B.D.L.	B.D.L.	1.45	0.36
Eu	0.05	B.D.L.	B.D.L.	0.07	0.02	B.D.L.	B.D.L.	0.10	0.02
Gd	0.18	B.D.L.	0.19	1.74	0.58	B.D.L.	B.D.L.	1.21	0.32
Tb	0.06	B.D.L.	B.D.L.	0.12	0.04	B.D.L.	B.D.L.	0.09	0.03
Dy	0.20	B.D.L.	B.D.L.	1.45	0.48	B.D.L.	B.D.L.	1.02	0.26
Ho	0.08	B.D.L.	B.D.L.	0.20	0.07	B.D.L.	B.D.L.	0.14	0.04
Er	0.15	B.D.L.	B.D.L.	0.46	0.15	B.D.L.	B.D.L.	0.48	0.13
Tm	0.09	B.D.L.	B.D.L.	0.14	0.05	B.D.L.	B.D.L.	B.D.L.	0.00
Yb	0.19	B.D.L.	B.D.L.	1.01	0.34	B.D.L.	B.D.L.	0.20	0.06
Lu	0.08	B.D.L.	B.D.L.	0.14	0.05	B.D.L.	B.D.L.	B.D.L.	0.00
Hf	0.07	0.11	0.11	0.11	0.00	0.11	0.11	0.18	0.02
Ta	0.07	0.05	0.31	0.81	0.29	B.D.L.	0.15	0.32	0.08
W	0.49	B.D.L.	B.D.L.	B.D.L.	0.00	B.D.L.	B.D.L.	B.D.L.	0.00
Au	0.03	B.D.L.	B.D.L.	B.D.L.	0.00	B.D.L.	B.D.L.	B.D.L.	0.00
Pb	0.44	B.D.L.	B.D.L.	0.71	0.15	B.D.L.	B.D.L.	0.84	0.15
Th	0.31	B.D.L.	B.D.L.	2.03	0.67	B.D.L.	1.06	3.30	1.06
U	0.11	B.D.L.	B.D.L.	0.29	0.10	B.D.L.	0.26	0.90	0.27

Table 2. (Cont.)

Laco Norte									
	D.L.	Drill core: Intermediate depths Magnetite X and Y N = 21				Drill core: Shallow Magnetite Z N = 14			
		Min.	Mean	Max.	Std. Dev	Min.	Mean	Max.	Std. Dev
		EPMA							
Fe (wt %)	0.02	66.47	69.44	70.91	1.36	67.82	70.02	70.93	1.00
Ti (ppm)	89.46	1,672.83	2,782.03	6,271.75	1,245.11	900.00	1,264.29	1,800.00	264.89
V (ppm)	66.39	793.81	894.98	1,090.07	85.19	800.00	957.14	1,000.00	64.62
Al (ppm)	81.24	1,575.32	2,722.70	4,287.65	773.80	1,562.00	2,069.14	2,670.00	302.57
Mn (ppm)	80.45	B.D.L.	372.04	933.76	263.33	B.D.L.	228.57	500.00	216.36
Mg (ppm)	128.04	5,021.56	8,564.88	13,962.82	2,825.28	1,000.00	7,121.43	8,900.00	2,393.00
Si (ppm)	68.07	76.68	3,825.26	11,895.99	4,221.33	100.00	235.71	900.00	227.38
P (ppm)	83.51	B.D.L.	B.D.L.	B.D.L.	0.00	B.D.L.	B.D.L.	200.00	53.45
Ca (ppm)	83.73	B.D.L.	1271.86	3789.22	1,454.62	B.D.L.	B.D.L.	B.D.L.	0.00
Cr (ppm)	62.61	B.D.L.	B.D.L.	B.D.L.	0.00	B.D.L.	B.D.L.	B.D.L.	0.00
LA-ICP-MS (ppm)	D.L. (ppm)								
Na	56.67	B.D.L.	553.39	2130.00	661.98	B.D.L.	B.D.L.	207.00	48.30
Mg	43.53	5,750.00	9,442.38	14,240.00	2,605.09	5,520.00	7,422.14	9,740.00	1,610.30
Al	36.52	3,660.00	6,492.38	9,100.00	1,387.52	1,562.00	2,069.14	2,670.00	302.57
Si	2,989.50	B.D.L.	8,861.29	28,400.00	7,953.87	B.D.L.	10,167.09	69,000.00	18,120.91
P	9.57	10.00	48.44	134.00	37.56	10.16	953.61	9,100.00	2,399.61
K	35.84	B.D.L.	627.05	3,130.00	836.92	B.D.L.	B.D.L.	165.00	47.39
Ca	738.79	B.D.L.	2,288.56	9,020.00	2,491.09	B.D.L.	1,630.15	9,900.00	2,640.57
Sc	4.90	B.D.L.	B.D.L.	8.80	1.99	B.D.L.	3.76	11.20	2.16
Ti	37.26	2,040.00	3,363.38	5,240.00	878.31	B.D.L.	1,410.93	2,040.00	277.74
V	14.33	1,688.00	2,027.52	2,590.00	248.24	1,830.00	2,158.71	2,410.00	149.93
Cr	3.40	B.D.L.	B.D.L.	6.80	1.04	B.D.L.	B.D.L.	5.20	0.80
Mn	5.59	313.00	561.95	829.00	120.04	122.30	428.16	677.00	152.55
Co	2.13	143.90	155.07	170.00	6.91	89.00	137.79	162.00	20.01
Ni	4.44	272.00	306.38	338.00	18.55	278.00	305.07	350.00	16.96
Cu	1.76	B.D.L.	B.D.L.	B.D.L.	0.00	B.D.L.	B.D.L.	B.D.L.	0.00
Zn	5.57	21.10	47.79	112.00	19.80	41.50	70.38	107.00	17.95
Ga	0.94	34.20	46.26	57.50	6.68	25.00	27.33	30.20	1.68
Ge	2.19	B.D.L.	2.91	4.50	0.86	B.D.L.	2.37	3.90	0.72
As	5.51	B.D.L.	B.D.L.	5.60	2.04	B.D.L.	B.D.L.	38.00	10.03
Rb	1.09	B.D.L.	2.09	22.50	4.90	B.D.L.	B.D.L.	B.D.L.	0.00
Sr	0.08	B.D.L.	3.40	13.80	4.47	B.D.L.	2.00	14.20	3.70
Y	0.99	B.D.L.	2.99	13.70	3.92	B.D.L.	B.D.L.	2.54	0.62
Zr	0.08	0.44	7.80	22.30	7.73	0.44	0.55	1.18	0.22
Nb	0.27	B.D.L.	1.48	4.63	1.52	B.D.L.	B.D.L.	0.45	0.10
Mo	1.42	0.45	1.51	4.50	0.75	B.D.L.	1.70	2.60	0.41
Ag	1.73	B.D.L.	B.D.L.	1.76	0.37	B.D.L.	B.D.L.	B.D.L.	0.00
Cd	0.36	B.D.L.	B.D.L.	B.D.L.	0.00	B.D.L.	B.D.L.	B.D.L.	0.00
Sn	0.95	4.58	6.00	8.10	1.20	4.03	5.44	7.20	0.82
Sb	1.28	B.D.L.	B.D.L.	B.D.L.	0.00	B.D.L.	B.D.L.	B.D.L.	0.00
Ba	0.15	B.D.L.	6.92	26.70	8.88	B.D.L.	4.48	34.00	9.66
La	0.21	B.D.L.	4.57	29.10	7.75	B.D.L.	3.92	29.00	7.53
Ce	0.46	B.D.L.	10.19	53.90	15.28	B.D.L.	9.56	73.00	18.98
Pr	0.07	B.D.L.	0.96	3.84	1.24	B.D.L.	0.90	7.80	2.04
Nd	0.27	B.D.L.	3.32	13.30	4.26	B.D.L.	2.71	24.10	6.31
Sm	0.25	B.D.L.	0.42	2.03	0.63	B.D.L.	B.D.L.	3.10	0.82
Eu	0.05	B.D.L.	B.D.L.	0.27	0.08	B.D.L.	B.D.L.	0.27	0.07
Gd	0.18	B.D.L.	0.34	1.38	0.48	B.D.L.	0.19	2.26	0.60
Tb	0.06	B.D.L.	B.D.L.	0.23	0.07	B.D.L.	B.D.L.	0.30	0.08
Dy	0.20	B.D.L.	0.41	2.05	0.63	B.D.L.	B.D.L.	1.42	0.38
Ho	0.08	B.D.L.	0.08	0.34	0.12	B.D.L.	B.D.L.	0.22	0.06
Er	0.15	B.D.L.	0.22	1.52	0.43	B.D.L.	B.D.L.	0.23	0.06
Tm	0.09	B.D.L.	B.D.L.	0.20	0.05	B.D.L.	B.D.L.	B.D.L.	0.00
Yb	0.19	B.D.L.	0.35	2.00	0.53	B.D.L.	B.D.L.	B.D.L.	0.00
Lu	0.08	B.D.L.	B.D.L.	0.19	0.05	B.D.L.	B.D.L.	B.D.L.	0.00
Hf	0.07	0.11	0.11	0.12	0.00	0.11	0.11	0.11	0.00
Ta	0.07	0.05	0.15	0.43	0.11	B.D.L.	B.D.L.	B.D.L.	0.00
W	0.49	B.D.L.	0.78	5.90	1.54	B.D.L.	0.53	2.06	0.56
Au	0.03	B.D.L.	B.D.L.	B.D.L.	0.00	B.D.L.	B.D.L.	B.D.L.	0.00
Pb	0.44	B.D.L.	B.D.L.	0.49	0.07	B.D.L.	B.D.L.	B.D.L.	0.00
Th	0.31	B.D.L.	1.44	7.01	1.95	B.D.L.	1.31	6.40	1.58
U	0.11	B.D.L.	0.46	1.87	0.68	B.D.L.	0.22	1.16	0.37

Table 2. (Cont.)

Cristales Grandes									
	D.L.	Magnetite S1 N̄ = 49				Magnetite A N̄ = 69			
		Min.	Mean	Max.	Std. Dev	Min.	Mean	Max.	Std. Dev
EPMA									
Fe (wt %)	0.02	67.0	69.2	71.4	1.1	65.5	69.0	70.9	1.2
Ti (ppm)	89.46	104.0	3,981.6	7,346.0	2,155.2	B.D.L.	1,039.2	6,554.0	1,605.7
V (ppm)	66.39	848.0	1,677.3	1,983.0	200.4	1,151.0	1,653.6	1,875.0	170.3
Al (ppm)	81.24	674.0	3,420.6	8,103.0	1,468.8	532.0	1,459.8	5,162.0	1,101.4
Mn (ppm)	80.45	439.0	821.5	1,459.0	179.2	B.D.L.	716.3	1,009.0	211.6
Mg (ppm)	128.04	2,067.0	6,854.4	12,313.0	2,268.7	1,284.0	10,735.8	22,613.0	3,553.1
Si (ppm)	68.07	597.0	4,736.6	15,724.0	3,007.6	174.0	5,430.6	14,983.0	3,017.8
P (ppm)	83.51	B.D.L.	B.D.L.	B.D.L.	B.D.L.	B.D.L.	B.D.L.	211.0	20.4
Ca (ppm)	83.73	B.D.L.	1,411.6	3423.0	871.2	B.D.L.	1,881.0	4,904.0	1,239.7
Cr (ppm)	62.61	B.D.L.	54.6	100.0	27.2	B.D.L.	B.D.L.	122.0	21.8
LA-ICP-MS (ppm)									
Na	56.67	B.D.L.	404.9	1,110.0	260.6	B.D.L.	376.3	956.0	209.9
Mg	43.53	4,120.0	7,281.6	13,110.0	2,034.6	4,840.0	10,461.3	14,600.0	2,821.4
Al	36.52	712.0	3,483.0	6,140.0	1,706.0	604.0	1,663.9	4,860.0	1,120.3
Si	2,989.50	100.0	5,342.3	11,900.0	2,940.9	200.0	6,856.9	20,700.0	3,867.3
P	9.57	B.D.L.	40.2	134.0	43.2	B.D.L.	229.7	13,110.0	1,573.9
K	35.84	B.D.L.	193.8	1,570.0	258.9	B.D.L.	125.9	1,890.0	244.9
Ca	738.79	B.D.L.	1417.9	5,290.0	1,294.7	B.D.L.	2,285.2	22,800.0	2,795.2
Sc	4.90	B.D.L.	2.9	12.9	1.8	B.D.L.	3.0	10.4	1.5
Ti	37.26	99.0	4,292.8	7,650.0	2,749.6	277.0	1,270.7	7290.0	1,594.3
V	14.33	1,415.0	1759.2	2,050.0	192.5	1,397.0	1,795.7	2,100.0	182.2
Cr	3.40	B.D.L.	11.1	57.9	13.9	B.D.L.	B.D.L.	25.4	2.9
Mn	5.59	578.0	926.2	1,420.0	147.5	411.0	807.0	1162.0	210.7
Co	2.13	65.8	117.9	140.7	14.3	61.7	95.4	153.7	26.1
Ni	4.44	42.0	89.4	116.2	17.0	39.9	78.0	146.7	32.9
Cu	1.76	B.D.L.	8.5	44.5	10.2	B.D.L.	4.6	48.2	9.5
Zn	5.57	89.0	148.6	201.0	26.0	51.9	116.9	195.0	32.8
Ga	0.94	13.9	36.2	47.5	12.4	9.2	24.3	46.0	10.5
Ge	2.19	22.4	26.6	31.9	2.1	22.5	26.5	32.7	1.8
As	5.51	B.D.L.	B.D.L.	9.5	1.5	B.D.L.	B.D.L.	11.7	2.8
Rb	1.09	B.D.L.	B.D.L.	24.5	3.4	B.D.L.	1.4	38.4	4.7
Sr	0.08	0.3	5.9	19.5	4.6	0.3	4.8	59.6	7.7
Y	0.99	B.D.L.	9.8	214.0	30.3	B.D.L.	14.0	94.8	14.4
Zr	0.08	0.5	3.5	77.0	10.8	B.D.L.	2.6	9.1	1.4
Nb	0.27	1.1	3.5	40.6	7.9	0.8	16.6	44.1	16.2
Mo	1.42	B.D.L.	B.D.L.	B.D.L.	B.D.L.	B.D.L.	B.D.L.	1.8	0.1
Ag	1.73	B.D.L.	B.D.L.	B.D.L.	B.D.L.	B.D.L.	B.D.L.	B.D.L.	B.D.L.
Cd	0.36	B.D.L.	0.4	1.8	0.2	B.D.L.	B.D.L.	B.D.L.	B.D.L.
Sn	0.95	4.0	6.9	27.7	5.2	3.6	13.4	29.4	9.0
Sb	1.28	B.D.L.	0.9	3.5	0.7	B.D.L.	B.D.L.	2.0	0.3
Ba	0.15	B.D.L.	7.2	114.0	16.1	B.D.L.	3.9	44.3	6.7
La	0.21	0.4	9.3	76.7	14.5	0.9	33.8	168.0	32.9
Ce	0.46	0.6	22.4	199.0	37.5	1.3	82.5	342.0	79.8
Pr	0.07	B.D.L.	2.6	21.8	4.0	B.D.L.	9.2	42.7	9.0
Nd	0.27	B.D.L.	9.7	61.4	12.4	B.D.L.	29.8	167.0	29.8
Sm	0.25	B.D.L.	1.5	7.7	1.7	B.D.L.	4.0	30.9	4.5
Eu	0.05	B.D.L.	0.1	0.7	0.2	B.D.L.	0.4	1.7	0.4
Gd	0.18	B.D.L.	1.7	13.3	2.4	B.D.L.	4.1	31.2	4.5
Tb	0.06	B.D.L.	0.2	2.9	0.4	B.D.L.	0.4	3.2	0.5
Dy	0.20	B.D.L.	1.4	21.8	3.2	B.D.L.	2.6	19.4	2.8
Ho	0.08	B.D.L.	0.3	5.3	0.8	B.D.L.	0.5	3.5	0.5
Er	0.15	B.D.L.	1.0	18.6	2.7	B.D.L.	1.7	11.7	1.8
Tm	0.09	B.D.L.	0.1	2.7	0.4	B.D.L.	0.3	1.3	0.2
Yb	0.19	B.D.L.	1.0	13.6	2.0	B.D.L.	2.0	8.8	1.7
Lu	0.08	B.D.L.	0.2	2.7	0.4	B.D.L.	0.3	1.5	0.3
Hf	0.07	B.D.L.	0.1	0.9	0.1	B.D.L.	B.D.L.	B.D.L.	B.D.L.
Ta	0.07	B.D.L.	0.1	0.3	0.1	B.D.L.	0.2	0.6	0.2
Au	0.03	B.D.L.	B.D.L.	B.D.L.	B.D.L.	B.D.L.	B.D.L.	0.0	0.0
Pb	0.44	B.D.L.	0.4	3.3	0.5	B.D.L.	B.D.L.	2.0	0.3
Th	0.31	B.D.L.	5.6	65.0	13.4	B.D.L.	30.0	101.0	29.8
U	0.11	B.D.L.	0.9	10.0	2.2	0.2	3.9	12.7	3.8

Table 2. (Cont.)

Rodados Negros		Magnetite S2 N = 104				Magnetite A N = 1
	D.L.	Min.	Mean	Max.	Std. dev	
<u>EPMA</u>						
Fe (wt %)	0.02	68.2	70.5	71.5	0.6	69.8
Ti (ppm)	89.46	B.D.L.	364.4	1,662.0	375.7	103.0
V (ppm)	66.39	259.0	1,050.3	1,447.0	284.2	274.0
Al (ppm)	81.24	126.0	917.7	3,327.0	721.0	884.0
Mn (ppm)	80.45	642.0	968.0	1,404.0	215.0	927.0
Mg (ppm)	128.04	5,881.0	7,739.0	19,610.0	1,705.4	7,406.0
Si (ppm)	68.07	107.0	1,809.5	12,190.0	2,196.5	609.0
P (ppm)	83.51	B.D.L.	B.D.L.	B.D.L.	B.D.L.	B.D.L.
Ca (ppm)	83.73	B.D.L.	481.0	2,782.0	726.2	B.D.L.
Cr (ppm)	62.61	B.D.L.	B.D.L.	81.0	10.6	B.D.L.
<u>LA-ICP-MS (ppm)</u>						
Na	56.67	B.D.L.	122.7	761.0	160.0	78.0
Mg	43.53	6,100.0	7,710.1	11,490.0	1,166.7	7,280.0
Al	36.52	155.3	1,074.4	3,620.0	882.1	345.0
Si	2,989.50	B.D.L.	4,378.3	13,700.0	3,244.5	8,300.0
P	9.57	B.D.L.	58.0	1,600.0	169.1	58.0
K	35.84	B.D.L.	37.9	224.0	46.9	B.D.L.
Ca	738.79	B.D.L.	934.2	3,780.0	889.2	B.D.L.
Sc	4.90	B.D.L.	B.D.L.	11.8	1.2	B.D.L.
Ti	37.26	60.0	454.9	1,840.0	450.6	103.0
V	14.33	311.0	1,112.5	1,499.0	289.8	266.0
Cr	3.40	B.D.L.	B.D.L.	30.7	3.6	B.D.L.
Mn	5.59	723.0	1,055.4	1,520.0	223.2	1017.0
Co	2.13	100.4	132.3	165.5	16.2	147.1
Ni	4.44	96.8	123.2	150.0	14.2	106.0
Cu	1.76	B.D.L.	B.D.L.	20.8	2.6	1.9
Zn	5.57	89.7	153.3	266.0	43.4	188.0
Ga	0.94	6.5	11.2	19.4	3.2	7.7
Ge	2.19	23.7	27.1	31.6	1.4	24.8
As	5.51	B.D.L.	B.D.L.	12.0	1.1	B.D.L.
Rb	1.09	B.D.L.	B.D.L.	1.1	0.1	B.D.L.
Sr	0.08	B.D.L.	1.0	7.1	1.8	B.D.L.
Y	0.99	B.D.L.	3.9	103.0	13.5	1.8
Zr	0.08	0.3	1.1	4.8	0.9	0.7
Nb	0.27	B.D.L.	1.6	7.5	1.7	1.1
Mo	1.42	B.D.L.	B.D.L.	1.6	0.1	B.D.L.
Ag	1.73	B.D.L.	B.D.L.	B.D.L.	B.D.L.	B.D.L.
Cd	0.36	B.D.L.	B.D.L.	B.D.L.	B.D.L.	B.D.L.
Sn	0.95	3.9	5.4	8.0	0.9	8.5
Sb	1.28	B.D.L.	B.D.L.	B.D.L.	B.D.L.	B.D.L.
Ba	0.15	B.D.L.	B.D.L.	8.7	1.7	B.D.L.
La	0.21	B.D.L.	4.2	20.4	5.9	B.D.L.
Ce	0.46	B.D.L.	8.2	48.7	12.3	0.8
Pr	0.07	B.D.L.	0.8	4.5	1.2	0.1
Nd	0.27	B.D.L.	2.8	12.2	3.7	B.D.L.
Sm	0.25	B.D.L.	0.5	3.0	0.6	B.D.L.
Eu	0.05	B.D.L.	0.1	1.4	0.2	B.D.L.
Gd	0.18	B.D.L.	0.7	11.3	1.4	B.D.L.
Tb	0.06	B.D.L.	0.1	0.9	0.1	B.D.L.
Dy	0.20	B.D.L.	0.6	11.9	1.6	0.3
Ho	0.08	B.D.L.	0.1	2.2	0.3	B.D.L.
Er	0.15	B.D.L.	0.4	11.9	1.3	0.3
Tm	0.09	B.D.L.	B.D.L.	0.9	0.1	B.D.L.
Yb	0.19	B.D.L.	0.4	6.9	1.0	B.D.L.
Lu	0.08	B.D.L.	B.D.L.	0.9	0.1	B.D.L.
Hf	0.07	B.D.L.	B.D.L.	0.3	0.0	B.D.L.
Ta	0.07	B.D.L.	B.D.L.	0.1	0.0	B.D.L.
Au	0.03	B.D.L.	B.D.L.	B.D.L.	B.D.L.	B.D.L.
Pb	0.44	B.D.L.	B.D.L.	B.D.L.	B.D.L.	B.D.L.
Th	0.31	B.D.L.	3.6	24.9	6.4	B.D.L.
U	0.11	B.D.L.	0.3	2.3	0.5	B.D.L.

Table 2. (Cont.)

San Vicente Alto									
		Magnetite S2 N = 23				Magnetite A N = 44			
	D.L.	Min.	Mean	Max.	Std. Dev	Min.	Mean	Max.	Std. Dev
EPMA									
Fe (wt %)	0.02	67.5	69.2	71.2	1.2	66.4	67.9	69.9	0.5
Ti (ppm)	89.46	B.D.L.	123.3	243.0	60.8	B.D.L.	156.4	345.0	90.6
V (ppm)	66.39	620.0	873.8	979.0	95.3	668.0	902.3	1,091.0	83.6
Al (ppm)	81.24	B.D.L.	737.3	2311.0	629.6	282.0	922.8	4,500.0	708.6
Mn (ppm)	80.45	B.D.L.	473.8	684.0	173.7	B.D.L.	292.8	629.0	203.6
Mg (ppm)	128.04	417.0	6,668.2	10,600.0	2,335.5	B.D.L.	4,324.1	39,018.0	6,281.4
Si (ppm)	68.07	64.4	411.3	688.0	200.2	306.0	3,750.4	11,907.0	2,881.6
P (ppm)	83.51	B.D.L.	205.3	1,109.0	313.9	B.D.L.	256.0	2,194.0	461.1
Ca (ppm)	83.73	B.D.L.	738.2	1,879.0	626.9	B.D.L.	377.9	2,063.0	554.0
Cr (ppm)	62.61	B.D.L.	B.D.L.	B.D.L.	0.0	B.D.L.	B.D.L.	73.0	9.9
LA-ICP-MS (ppm)	D.L. (ppm)								
Na	56.67	B.D.L.	168.3	451.0	162.3	B.D.L.	142.9	584.0	209.0
Mg	43.53	635.0	4,533.3	7,980.0	2,440.8	180.0	3,147.4	8,580.0	2,938.0
Al	36.52	64.4	411.3	688.0	200.2	196.0	527.7	974.0	237.5
Si	2,989.50	B.D.L.	4,677.6	17,600.0	4,139.0	B.D.L.	4,163.5	14,000.0	2,756.3
P	9.57	12.0	111.9	449.0	120.1	B.D.L.	102.7	344.0	106.2
K	35.84	B.D.L.	47.5	113.3	34.1	B.D.L.	41.1	150.0	45.7
Ca	738.79	B.D.L.	852.7	2,470.0	700.3	B.D.L.	B.D.L.	1,960.0	461.3
Sc	4.90	B.D.L.	B.D.L.	B.D.L.	0.0	B.D.L.	B.D.L.	B.D.L.	0.0
Ti	37.26	17.7	149.4	250.0	76.5	49.4	185.5	350.0	90.7
V	14.33	532.0	906.5	1,082.0	130.5	725.0	916.1	1,095.0	87.2
Cr	3.40	B.D.L.	B.D.L.	B.D.L.	0.0	B.D.L.	B.D.L.	B.D.L.	0.0
Mn	5.59	77.0	391.3	746.0	221.1	38.7	307.5	646.0	191.5
Co	2.13	88.6	129.7	156.4	19.3	78.6	119.5	154.0	22.8
Ni	4.44	175.4	245.2	287.0	29.5	182.6	242.6	293.0	27.0
Cu	1.76	B.D.L.	10.6	61.1	18.1	B.D.L.	10.2	93.4	21.1
Zn	5.57	20.3	61.6	95.4	23.1	18.5	57.3	90.9	21.5
Ga	0.94	B.D.L.	2.2	3.8	1.0	B.D.L.	2.4	4.1	0.8
Ge	2.19	21.0	22.9	26.2	1.3	21.2	23.8	26.9	1.3
As	5.51	B.D.L.	B.D.L.	7.1	0.9	B.D.L.	B.D.L.	B.D.L.	0.0
Rb	1.09	B.D.L.	B.D.L.	B.D.L.	0.0	B.D.L.	B.D.L.	B.D.L.	0.0
Sr	0.08	0.4	1.9	4.0	1.0	0.2	1.7	5.5	1.2
Y	0.99	B.D.L.	2.4	7.5	2.1	B.D.L.	1.8	4.2	0.9
Zr	0.08	B.D.L.	4.7	98.0	20.3	0.3	0.6	1.6	0.3
Nb	0.27	0.8	5.0	14.5	3.8	0.8	4.1	11.1	2.7
Mo	1.42	B.D.L.	B.D.L.	4.3	0.9	B.D.L.	B.D.L.	1.9	0.3
Ag	1.73	B.D.L.	B.D.L.	B.D.L.	0.0	B.D.L.	B.D.L.	B.D.L.	0.0
Cd	0.36	B.D.L.	B.D.L.	B.D.L.	0.0	B.D.L.	B.D.L.	B.D.L.	0.0
Sn	0.95	3.2	4.0	5.6	0.7	2.9	3.8	4.4	0.4
Sb	1.28	B.D.L.	B.D.L.	B.D.L.	0.0	B.D.L.	B.D.L.	B.D.L.	0.0
Ba	0.15	0.2	7.4	47.2	13.0	B.D.L.	9.0	118.1	19.8
La	0.21	1.0	5.3	18.7	5.3	0.8	3.3	7.9	1.9
Ce	0.46	1.8	9.8	31.6	9.2	1.9	6.5	15.5	3.4
Pr	0.07	0.2	1.0	3.3	0.9	0.2	0.7	1.6	0.4
Nd	0.27	0.6	3.5	11.1	3.2	0.7	2.4	5.3	1.2
Sm	0.25	B.D.L.	0.5	1.5	0.5	B.D.L.	0.4	0.9	0.2
Eu	0.05	B.D.L.	0.1	0.2	0.1	B.D.L.	B.D.L.	0.1	0.0
Gd	0.18	B.D.L.	0.5	1.4	0.4	B.D.L.	0.4	0.9	0.2
Tb	0.06	B.D.L.	0.1	0.2	0.1	B.D.L.	B.D.L.	0.1	0.0
Dy	0.20	B.D.L.	0.4	1.1	0.3	B.D.L.	0.3	0.7	0.2
Ho	0.08	B.D.L.	0.1	0.4	0.1	B.D.L.	B.D.L.	0.2	0.0
Er	0.15	B.D.L.	0.2	0.9	0.2	B.D.L.	0.2	0.4	0.1
Tm	0.09	B.D.L.	B.D.L.	0.1	0.0	B.D.L.	B.D.L.	B.D.L.	0.0
Yb	0.19	B.D.L.	0.3	0.8	0.2	B.D.L.	0.2	0.6	0.2
Lu	0.08	B.D.L.	B.D.L.	0.2	0.0	B.D.L.	B.D.L.	0.1	0.0
Hf	0.07	B.D.L.	0.1	1.2	0.2	B.D.L.	B.D.L.	B.D.L.	0.0
Ta	0.07	B.D.L.	0.3	1.1	0.2	B.D.L.	B.D.L.	0.7	0.2
Au	0.03	B.D.L.	B.D.L.	B.D.L.	0.0	B.D.L.	B.D.L.	B.D.L.	0.0
Pb	0.44	B.D.L.	B.D.L.	0.7	0.1	B.D.L.	B.D.L.	0.5	0.0
Th	0.31	0.6	6.8	23.4	7.3	0.4	3.5	10.7	2.7
U	0.11	B.D.L.	0.5	2.5	0.6	B.D.L.	B.D.L.	1.8	0.6

Abbreviation: B.D.L. = below detection limit

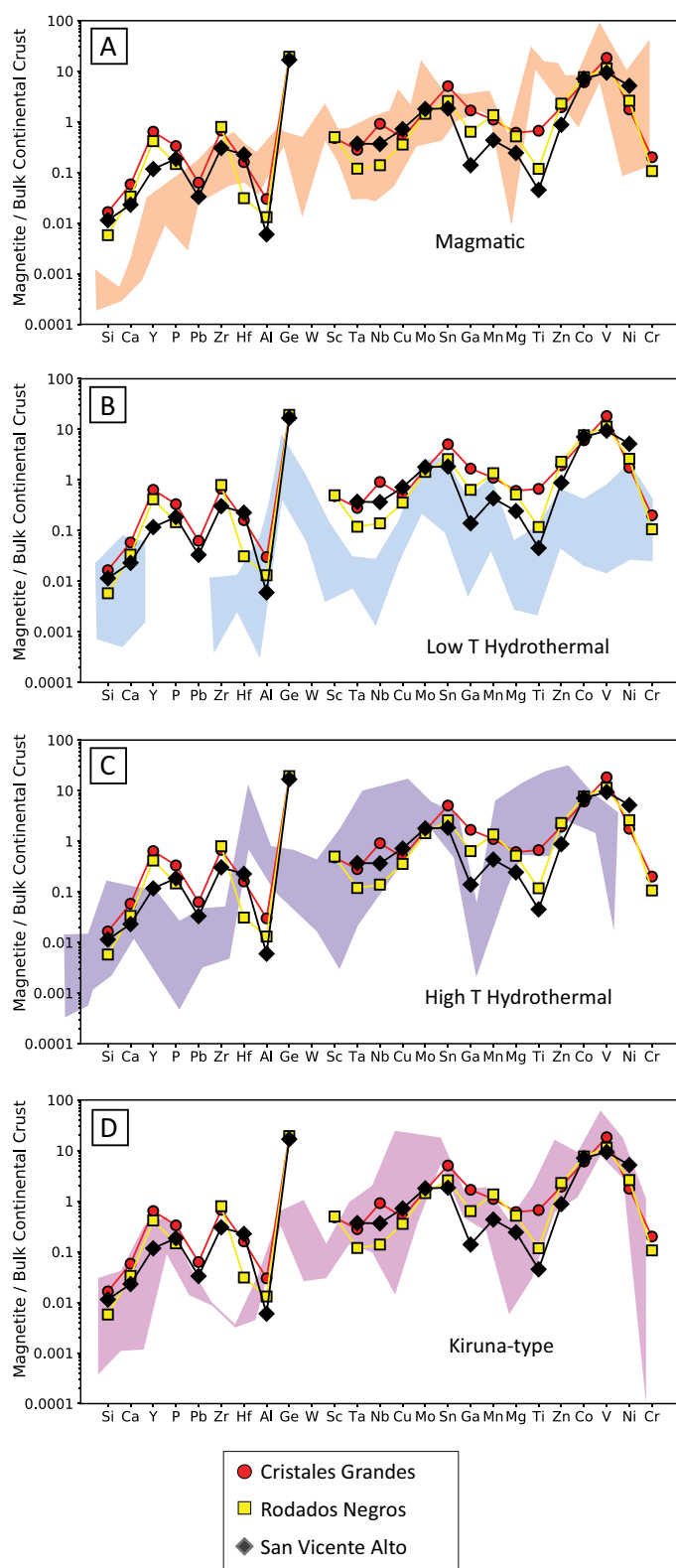


Fig. 4. The compositions of magnetite from Cristales Grandes, Rodados Negros, and San Vicente Alto (lines) compared to the range of magnetite compositions (fields) from (A) igneous rocks, (B) low-temperature hydrothermal environments, (C) magmatic-hydrothermal environments, and (D) Kiruna-type IOA deposits. All compositions are normalized to average bulk continental crust using values in Rudnick and Gao (2003). Fields are taken from Dare et al. (2014) and Knipping et al. (2015b). W was not measured.

1 and the minimum, maximum, and average compositions are presented in Table 3. The concentrations of Ti, Sc, Cr, Co, Cu, Zn, Nb, Mo, Xe, W, and Os were below the limit of detection for the majority of the analyses. Apatite from Cristales Grandes and Laco Sur is fluorapatite (Fig. 8). Apatite from Rodados Negros exhibits a larger range of fluorine and chlorine concentrations, with the porous/mottled regions in apatite grains containing higher concentrations of chlorine (up to ~2.1 wt %) compared to visually homogeneous portions of the apatite grains that contain lower chlorine concentrations (~1.1 wt %); these grains are compositionally chlor-fluorapatite. For apatite from Cristales Grandes, regions with purple luminescence have higher concentrations of Na, V, Fe, Th, and total REEs, while the regions with blue luminescence have higher concentrations of Si. The regions of mauve luminescence in apatite at Rodados Negros have higher concentrations of F, calculated OH, Th, and total REEs, while the regions of orange luminescence have higher iron and chlorine contents. For the fluorapatite from Laco Sur, the regions with dark luminescence have higher average sulfur (8,089 ppm) and iron contents than the regions with purple/blue luminescence.

Discussion

Magnetite minor and trace element compositions

Magnetite has inverse spinel structure with tetrahedral and octahedral sites that accommodate ferric iron, and ferric and ferrous iron, respectively. The two cation sites in magnetite allow it to incorporate a wide range of cations that substitute for ferric and ferrous iron based on charge and size considerations (Dupuis and Beaudoin, 2011; Nadoll et al., 2014). Comprehensive investigations of the minor and trace element composition of magnetite from mineral systems in which the temperature of magnetite crystallization is inferred from the homogenization temperatures of fluid inclusions hosted in paragenetically equivalent phases, such as quartz and calcite, were used by Nadoll et al. (2014) to propose a discriminant diagram that distinguishes magnetite from different ore deposits based on minor and trace element chemistry. This discriminant diagram allows the chemical composition of magnetite to be used to approximate its temperature of crystallization. Generally, the minor and trace element content of magnetite that crystallizes from silicate melt or hydrothermal fluid decreases as the temperature of the fluid decreases (Nadoll et al., 2014). The use of the discriminant diagram of Nadoll et al. (2014) and comparisons of our data to that from other studies that investigate magnetite chemistry from different environments (e.g., Dupuis and Beaudoin, 2011; Dare et al., 2014; Knipping et al., 2015b; Wen et al., 2017) allow us to gain insights about the evolution of the temperatures of the ore fluids that can then be linked to genetic processes for understanding ore genesis.

Surface to depth chemical variability of magnetite

The concentrations of minor and trace elements in magnetite decrease systematically from depth to surface for drill core samples from Laco Norte and Laco Sur (Fig. 6D). In surface samples, titanium concentrations are highest at Cristales Grandes and progressively decrease in samples from Rodados Negros to San Vicente Alto (Figs. 3A, 6). The average titanium

Table 3. Summary of Compositions of Apatite from Outcrop Samples at Cristales Grandes, Rodados Negros, and Laco Sur

Cristales Grandes									
	D.L.	Purple luminescence/ Gray in BSE N = 145				Blue luminescence/ Light gray in BSE N = 12			
		Min.	Mean	Max.	Std. Dev	Min.	Mean	Max.	Std. Dev
EPMA									
CaO (wt %)	0.09	49.87	53.43	54.68	0.88	52.33	53.12	53.64	0.37
P ₂ O ₅ (wt %)	0.17	36.75	39.81	41.51	0.91	38.56	39.25	40.37	0.45
F (wt %)	0.27	2.06	3.16	3.98	0.22	2.89	3.10	3.44	0.18
Cl (wt %)	0.02	0.65	0.80	1.16	0.08	0.65	0.69	0.73	0.03
Calc. OH (wt %)	N/A	0.00	0.17	2.04	0.18	0.00	1.70	0.50	0.14
S (ppm)	155.50	B.D.L.	2,383.70	4,791.05	917.53	1,104.55	1,821.68	2,456.95	416.68
Si (ppm)	245.50	B.D.L.	2,923.29	4,781.43	1,078.02	3,183.10	4,876.86	5,487.07	628.34
Na (ppm)	369.50	B.D.L.	2,159.64	4,420.76	1,126.91	644.24	952.94	1,573.49	237.03
Al (ppm)	236.10	B.D.L.	B.D.L.	3,845.97	335.94	B.D.L.	B.D.L.	B.D.L.	B.D.L.
Mg (ppm)	250.30	B.D.L.	B.D.L.	368.63	106.71	B.D.L.	B.D.L.	B.D.L.	B.D.L.
Fe (ppm)	828.30	B.D.L.	B.D.L.	1,374.48	274.92	B.D.L.	B.D.L.	833.40	240.58
LA-ICP-MS (ppm) D.L. (ppm)									
Na	29.91	1,063.00	1,924.60	4,540.00	579.28	919.00	1,238.83	1,600.00	204.67
Mg	0.87	141.30	206.33	310.00	24.67	88.30	159.75	214.30	41.52
Al	5.24	B.D.L.	10.78	555.00	59.14	B.D.L.	3.00	7.10	1.29
Si	2,616.06	B.D.L.	6,453.76	66,200.00	7,012.24	B.D.L.	8,786.01	52,600.00	14,110.85
K	9.06	B.D.L.	11.82	300.00	28.45	B.D.L.	18.44	140.00	39.34
V	0.90	7.83	46.44	103.60	27.37	9.30	19.12	42.10	10.94
Mn	2.55	75.60	94.39	171.00	11.27	83.60	91.32	103.60	5.76
Fe	34.20	667.00	922.97	14,100.00	1,111.14	675.00	761.00	825.00	46.37
Ni	0.97	B.D.L.	2.07	6.00	0.81	B.D.L.	2.30	5.00	1.13
Ge	2.22	7.50	18.00	32.50	6.16	10.60	19.85	32.30	7.47
As	4.77	66.60	120.77	321.00	38.99	87.60	294.63	1,155.00	375.17
Sr	0.07	402.00	485.00	774.00	78.59	429.00	447.67	463.00	11.43
Y	0.05	280.00	759.95	1,270.00	280.99	474.00	793.08	1,132.00	232.25
Zr	0.05	B.D.L.	0.61	7.00	0.67	B.D.L.	0.49	1.24	0.43
Ba	0.10	0.32	1.13	3.70	0.50	0.57	0.93	1.59	0.34
La	0.10	2,673.00	4,279.85	8,670.00	1,189.10	3,030.00	4,297.58	6,240.00	1,210.80
Ce	0.06	2,456.97	4,004.35	6,265.04	879.70	4,210.00	6,355.00	9,840.00	2,109.12
Pr	0.02	256.00	570.53	1,352.00	213.13	342.00	571.75	984.00	218.25
Nd	0.08	767.00	1,901.03	4,200.00	686.57	1,172.00	1,904.50	3,190.00	722.88
Sm	0.06	91.80	299.53	1066.00	160.70	168.00	267.20	466.00	103.73
Eu	0.04	10.12	20.81	53.00	7.93	14.30	19.34	29.10	4.92
Gd	0.05	74.90	230.68	509.00	90.38	127.60	221.48	377.00	81.84
Tb	0.02	8.11	30.80	117.00	18.45	15.20	26.21	44.70	9.80
Dy	0.04	42.80	158.80	400.00	78.74	82.40	137.27	236.00	49.16
Ho	0.01	8.37	31.95	123.70	19.91	15.60	26.70	46.00	9.60
Er	0.03	20.80	81.61	335.00	52.01	37.50	67.56	110.40	23.29
Tm	0.02	2.45	11.41	54.40	8.20	4.80	8.49	14.80	3.00
Yb	0.05	14.40	65.68	337.00	49.27	32.40	50.26	85.40	16.25
Lu	0.01	2.05	11.51	135.70	18.81	4.38	6.22	11.42	2.10
Hf	0.03	B.D.L.	0.26	3.10	0.39	B.D.L.	0.17	0.33	0.10
Ta	0.01	B.D.L.	0.05	0.26	0.04	B.D.L.	0.06	0.19	0.05
Th	0.03	B.D.L.	561.10	17,100.00	1,458.91	174.90	323.06	625.00	132.66
U	0.01	B.D.L.	33.73	667.00	74.40	9.29	28.62	61.40	17.13
Total REEs	N/A	7,699.18	14,121.19	31,676.80	4,608.33	9,705.38	13,959.55	21,674.82	4,525.57
Rodados Negros									
	D.L.	Purple/mauve luminescence/ Non-porous apatite N = 59				Orange luminescence/ Mottled/porous apatite N = 11			
		Min.	Mean	Max.	Std. Dev	Min.	Mean	Max.	Std. Dev
EPMA									
CaO (wt %)	0.09	47.48	53.01	53.85	1.16	44.54	51.86	53.66	2.64
P ₂ O ₅ (wt %)	0.17	34.51	39.05	40.13	0.88	34.37	39.62	40.71	1.84
F (wt %)	0.27	2.33	3.10	3.64	0.27	2.07	2.51	2.86	0.23
Cl (wt %)	0.02	0.82	1.00	2.05	0.24	1.76	2.10	2.66	0.26
Calc. OH (wt %)	N/A	0.00	0.04	0.36	0.09	0.00	0.03	0.19	0.06
S (ppm)	155.50	0.00	2,080.64	3,806.84	1,207.70	0.00	1,922.42	3,777.30	1,396.56
Si (ppm)	245.50	0.00	2,674.70	8,304.48	1,530.96	0.00	2,749.31	7,105.50	2,037.85

Table 3. (Cont.)

Rodados Negros									
		Purple/mauve luminescence/ Non-porous apatite N = 59				Orange luminescence/ Mottled/porous apatite N = 11			
	D.L.	Min.	Mean	Max.	Std. Dev	Min.	Mean	Max.	Std. Dev
EPMA									
Na (ppm)	369.50	0.00	1,502.46	2,518.32	670.31	0.00	1,222.62	2,052.96	720.53
Al (ppm)	236.10	0.00	573.00	10,129.21	1884.19	0.00	4,669.78	49,579.36	14,898.38
Mg (ppm)	250.30	0.00	122.07	671.99	194.84	0.00	178.45	928.36	299.37
Fe (ppm)	828.30	0.00	940.65	6650.07	1638.36	0.00	3139.44	26934.56	8137.43
LA-ICP-MS (ppm)	D.L. (ppm)								
Na	29.91	1,126.00	1,582.10	2,282.00	307.55	847.00	1,459.82	2,100.00	420.96
Mg	0.87	130.50	186.49	292.00	41.06	135.40	314.04	650.00	130.96
Al	5.24	B.D.L.	270.99	2,680.00	586.73	B	1,229.15	2,420.00	813.01
Si	2,616.06	B.D.L.	5,123.54	27,700.00	3,755.01	B	3,720.37	5,800.00	1,762.39
K	9.06	B.D.L.	91.66	2,200.00	319.27	4.53	10.87	29.00	9.02
V	0.90	33.20	60.95	96.70	13.93	16.40	38.50	59.20	14.36
Mn	2.55	58.70	118.79	343.00	69.97	80.70	186.56	291.80	63.77
Fe	34.20	722.00	1,170.42	6,380.00	889.68	722.00	2,040.45	4,330.00	1,126.71
Ni	0.97	B.D.L.	2.91	10.20	1.82	B.D.L.	7.01	13.10	4.32
Ge	2.22	8.40	15.92	22.50	2.63	8.40	14.43	25.40	4.64
As	4.77	68.70	110.11	206.00	29.62	90.80	122.79	222.00	47.02
Sr	0.07	347.00	480.94	858.00	105.46	356.00	491.91	845.00	164.34
Y	0.05	420.00	582.23	1,057.00	122.51	402.00	527.82	800.00	144.16
Zr	0.05	B.D.L.	0.21	0.90	0.14	B.D.L.	0.14	0.33	0.10
Ba	0.10	0.35	6.51	101.00	15.45	0.98	17.95	87.00	24.17
La	0.10	2,160.00	3,852.32	7,540.00	1,502.55	1,250.00	3,235.27	6,530.00	1,845.79
Ce	0.06	3,520.00	5,725.33	11,010.00	2,136.71	2,330.00	4,905.45	9,480.00	2,499.70
Pr	0.02	297.00	485.97	1,097.00	217.11	240.00	448.64	935.00	237.87
Nd	0.08	888.00	1,324.58	2,490.00	406.99	701.00	1,208.36	2,070.00	464.03
Sm	0.06	117.20	170.11	298.00	43.00	110.80	165.80	282.00	55.18
Eu	0.04	11.15	18.33	36.00	7.02	11.74	20.82	32.60	7.43
Gd	0.05	95.20	156.68	306.00	55.55	95.20	163.97	270.00	54.83
Tb	0.02	10.08	16.82	37.00	6.35	10.51	18.04	30.70	6.68
Dy	0.04	47.80	81.15	184.00	29.96	52.00	88.35	138.20	30.36
Ho	0.01	10.17	16.14	34.60	5.21	10.76	17.06	27.10	5.57
Er	0.03	25.10	41.34	88.90	14.25	26.50	43.68	69.50	14.91
Tm	0.02	3.23	6.26	15.80	3.19	3.61	7.16	12.90	3.15
Yb	0.05	20.40	36.11	90.50	16.98	20.80	40.18	77.80	18.04
Lu	0.01	2.35	4.32	10.78	2.08	2.66	4.87	9.74	2.16
Hf	0.03	B.D.L.	0.09	0.33	0.07	B.D.L.	0.12	0.27	0.09
Ta	0.01	B.D.L.	0.02	0.07	0.01	B.D.L.	0.02	0.07	0.02
Th	0.03	128.90	395.33	1,690.00	383.04	43.50	421.50	1,430.00	488.42
U	0.01	8.68	23.18	80.30	17.82	5.75	23.62	64.50	20.03
Total REEs	N/A	7,390.27	11,935.48	22,604.39	4,419.18	4,961.99	10,367.67	19,911.34	5,204.54
Laco Sur									
		Bright luminescence/ Low S N = 62				Dark luminescence/ High S N = 23			
	D.L.	Min.	Mean	Max.	Std. Dev	Min.	Mean	Max.	Std. Dev
EPMA									
CaO (wt %)	0.09	51.67	54.47	55.51	0.58	50.46	53.27	55.06	1.09
P ₂ O ₅ (wt %)	0.17	39.11	41.16	42.80	0.72	37.64	39.40	40.53	0.82
F (wt %)	0.27	3.08	3.85	5.31	0.38	3.38	4.42	5.40	0.53
Cl (wt %)	0.02	0.26	0.55	0.74	0.12	B.D.L.	0.12	0.54	0.13
Calc. OH (wt %)	N/A	0.00	0.01	0.24	0.05	B.D.L.	0.01	0.10	0.02
S (ppm)	155.50	933.37	2,221.27	4,860.17	1,133.32	4,537.44	7997.11	11,341.79	1,655.10
Si (ppm)	245.50	382.37	731.29	1472.90	168.89	B.D.L.	378.93	1,005.46	283.66
Na (ppm)	369.50	873.17	2,425.37	6,265.75	1,114.42	3,910.34	5,831.25	8,479.46	1,185.61
Al (ppm)	236.10	B.D.L.	B.D.L.	B.D.L.	B.D.L.	B.D.L.	B.D.L.	B.D.L.	B.D.L.
Mg (ppm)	250.30	B.D.L.	B.D.L.	B.D.L.	B.D.L.	B.D.L.	B.D.L.	B.D.L.	B.D.L.
Fe (ppm)	828.30	4,733.82	7,626.55	13,312.21	1,955.31	6,553.50	11,379.85	41,628.06	6,967.74
Ce (ppm)	1,201.80	0.00	2,562.67	3786.47	668.44	B.D.L.	B.D.L.	2,037.10	735.68

Abbreviation: B.D.L. = below detection limit.

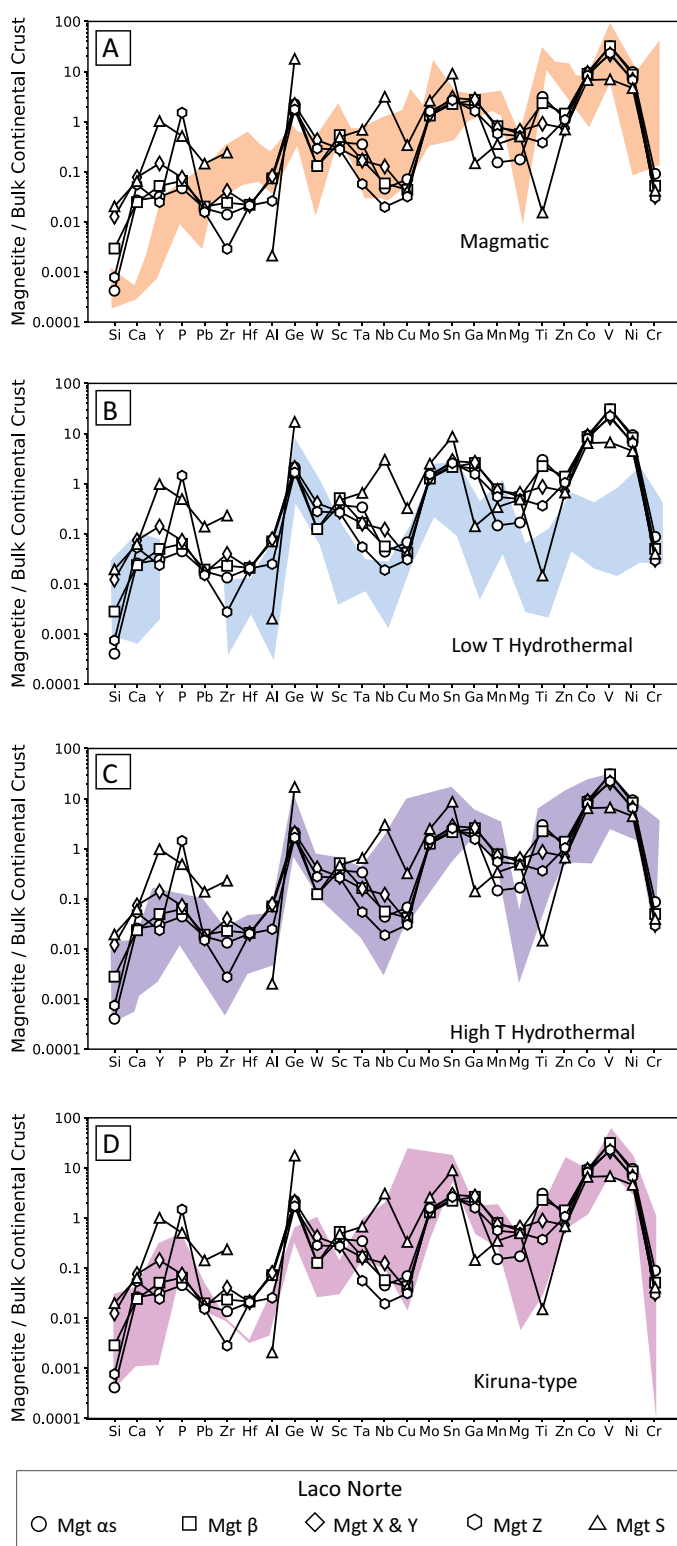


Fig. 5. Compositions of magnetite from outcrop and drill core samples from Laco Norte compared to the same fields shown in Figure 4. Magnetite- α and - β represent magnetite from the deep zone of the drill core, magnetite-X and -Y represent magnetite from intermediate depths in the deposit, magnetite-Z represents magnetite from shallow depths below the surface, and magnetite-S represents magnetite from outcrop samples.

concentrations in surface samples at Laco Sur and Laco Norte are 200 to 300 ppm and are generally consistent with published studies that focused on surface samples from El Laco (e.g., Nyström and Henriquez, 1994; Dare et al., 2015; Velasco et al., 2016; Broughm et al., 2017; Ovalle et al., 2018). However, the data reported here indicate that magnetite A and S1 from Cristales Grandes have average titanium concentrations of ~1,000 and ~4,000 ppm, and range up to ~7,300 ppm; these values are much higher than those reported in previous studies. The titanium concentrations reported here for magnetite from Cristales Grandes are consistent with Ovalle et al. (2018) who reported titanium concentrations >0.5 wt % in magnetite samples from deeper levels of Laco Sur and Laco Norte. Ovalle et al. (2018) reported that the titanium concentrations in surface samples from Laco Sur and Laco Norte are low, i.e., <0.1 wt %, but that magnetite at depths >100 m in those orebodies contains as much as >1 wt % Ti and also contain ilmenite oxyexsolution lamellae. The oxyexsolved ilmenite results from oxidation of titanomagnetite during cooling at temperatures above 600°C (Lindsley, 1962, 1963, 1991; Buddington and Lindsley, 1964; Haggerty, 1976, 1991; Tucker and O'Reilly, 1980). The ilmenite lamellae are not the product of exsolution *sensu stricto*, which requires unmixing of an original solid solution, such as magnetite-ulvöspinel, as that phase intersects the solvus during cooling. Rather, oxyexsolution of ilmenite is caused by oxidation of titanomagnetite without unmixing of a solid solution. Such oxidation at high temperature—when diffusion rates are high—in the presence of a fluid phase also explains the formation of interstitial ilmenite (Buddington and Lindsley, 1964; Haggerty, 1976). We highlight that the titanium concentrations measured by LA-ICP-MS in the current study are in good agreement with the titanium concentrations determined by EPMA (Ovalle et al., 2018; Fig. A3).

Generally, the concentrations of V, Mg, Al, Mn, Cr, and Ga in magnetite from surface samples are highest at Cristales Grandes and decrease progressively in samples from Rodados Negros and San Vicente Alto, following the same trend described above for Ti (Figs. 3, A1). The concentrations of Mn and Zn in magnetite are highest at Rodados Negros and are progressively lower in samples from Cristales Grandes and San Vicente Alto (Figs. 3, A1). For the drill core samples, the concentrations of Ti, V, Al, Mn, Ga, and Cr at Laco Sur and Laco Norte decrease systematically from depth to surface (Figs. 3, A1). The titanium and aluminum concentrations of magnetite from Cristales Grandes and the drill core samples from deep (150–200 m) and intermediate (65–145 m) depths are consistent with concentrations reported by Nadoll et al. (2014) for magnetite from igneous and high-temperature magmatic-hydrothermal environments (Figs. 6, A4). The V, Mn, and Cr concentrations of magnetite from all El Laco orebodies at all depths are similar to concentrations reported by Nadoll et al. (2014) for igneous and magmatic-hydrothermal magnetite, although the Cr content in magnetite from El Laco is generally low (Figs. 3, A1). The presence of titanium-enriched magnetite in the deeper parts of the orebodies (Fig. 2) and the systematic decrease of minor and trace element concentrations in magnetite from the orebodies (Fig. 6) suggest that both igneous and magmatic-hydrothermal processes played a role in forming the El Laco ore deposit.

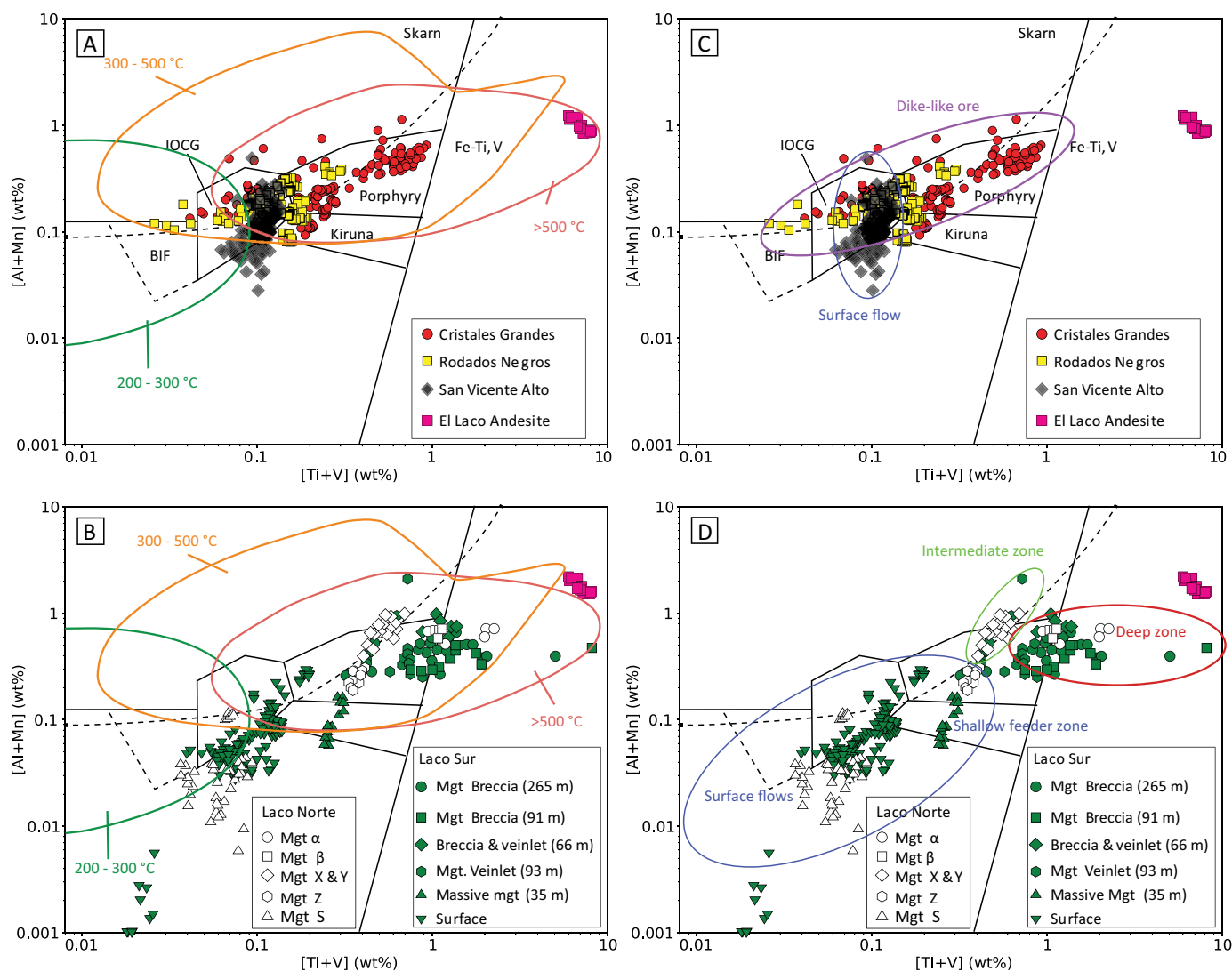


Fig. 6. $[Al + Mn]$ and $[Ti + V]$ for magnetite from El Laco orebodies and andesite (cf. Dare et al., 2015) plotted in the chemical discriminant diagram of Nadoll et al. (2014), with colored contours that represent magnetite formed at different temperatures (Nadoll et al., 2014). (A) contains data for outcrop samples from Cristales Grandes, Rodados Negros, and San Vicente Alto analyzed in this study, and (B) contains data for outcrop and drill core samples from Laco Norte and Laco Sur (depth in meters from surface given in parentheses). Explanation of magnetite types given in Table 1. In (C), we use ellipses to identify data from the dike-like orebodies at Cristales Grandes and Rodados Negros (purple ellipse; red circles and yellow squares) and the flow-like orebody at San Vicente Alto (blue ellipse; black diamonds). Finally, in (D), we identify magnetite from the deep breccia (red ellipse), the intermediate breccia (green ellipse), the shallow feeder zone (blue ellipse), and the surface flows (blue ellipse) from the Laco Sur and Laco Norte orebodies.

Comparison of El Laco magnetite geochemistry to magnetite from other environments

The compositions of magnetite at El Laco are compared in Figures 4, 5, and A2 with magnetite compositions from other Kiruna-type deposits, igneous rocks, and magnetite that crystallized from high- and low-temperature hydrothermal fluids in the multielement plots proposed by Dare et al. (2014). The compositional field for magmatic magnetite comprises data for magnetite that crystallized from silicate melts of intermediate and felsic compositions (Dare et al., 2014). The field for low-temperature hydrothermal magnetite comprises data for magnetite from banded iron formations (BIFs), and Fe-rich skarns, whereas the field for high-temperature hydrothermal

magnetite comprises data for magnetite from iron oxide-copper-gold (IOCG) and porphyry Cu deposits (Dare et al., 2014). The compositional field for Kiruna-type magnetite comprises data for magnetite from the El Laco, El Romeral, and Kiirunavaara IOA deposits.

The magnetite compositions reported here are most consistent with magnetite formed in magmatic-hydrothermal environments. There is also considerable overlap with the data for igneous magnetite (Figs. 4, 5, A2). The continental-crust normalized concentrations of all plotted elements overlap the field for high-temperature hydrothermal environments, except for Si, Ca, Y, Mg, P, Zr, Hf, and Ge that are slightly elevated, and Ga and Ti that are slightly depleted, relative

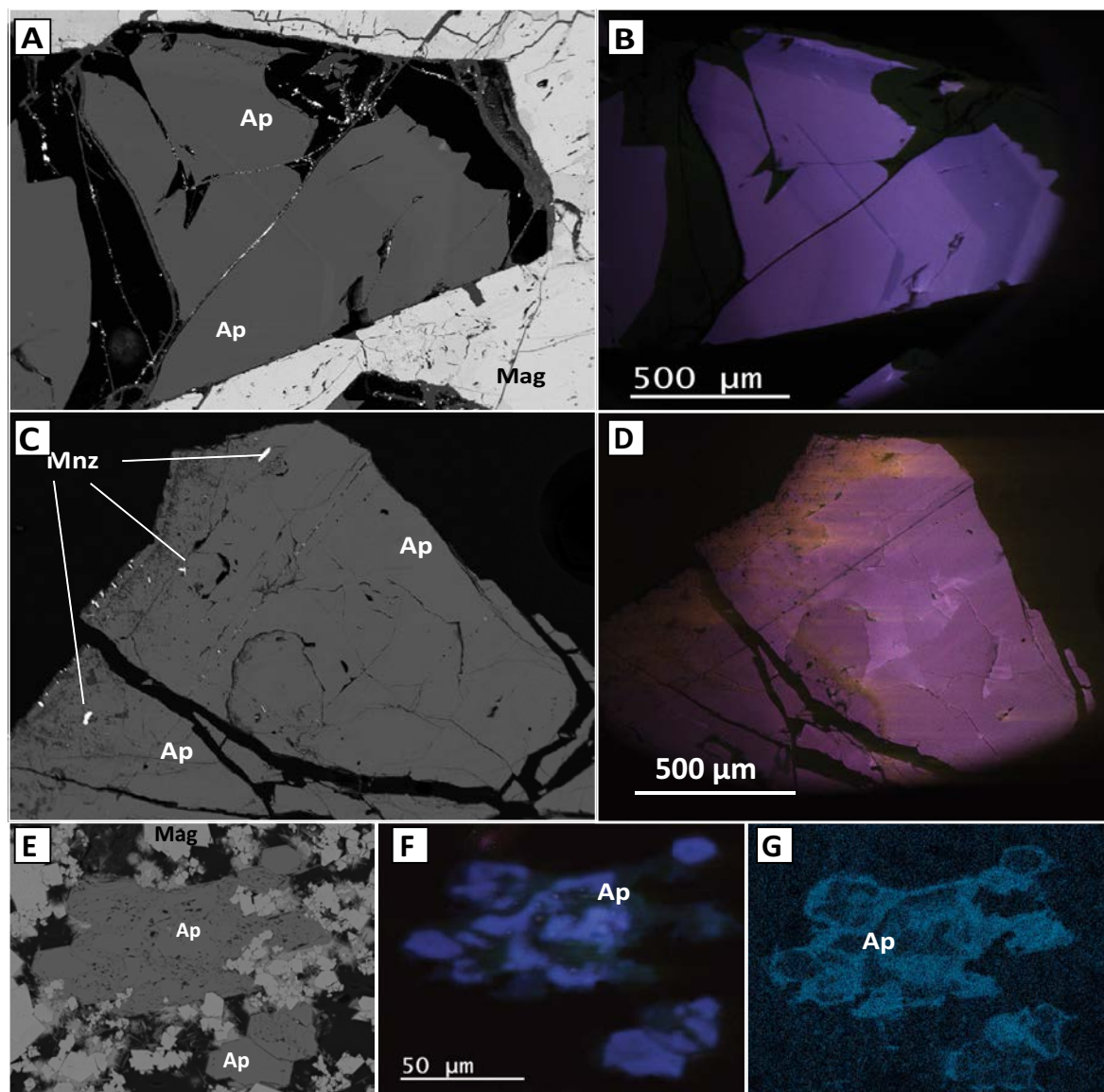


Fig. 7. Representative BSE and cathodoluminescence (CL) images for apatite from the El Laco orebodies. BSE (A) and CL (B) images of apatite from Cristales Grandes. Areas of dark luminescence in (B) correspond to brighter regions in the BSE image. BSE (C) and CL (D) images for apatite from Rodados Negros. Monazite grains (Mnz) occur in cracks within grains and at grain boundaries. The regions of orange luminescence in (D) correspond to regions within the apatite grains that have porous/mottled texture, higher chlorine contents, and contain monazite inclusions. BSE image (E), CL image (F), and sulfur K α EDS element map (G) for apatite grains from Laco Sur. The S K α map (G) reveals elevated sulfur concentrations near grain rims and regions of the grains with porous/mottled texture. Regions of low sulfur content in the apatite grains exhibit bright (purple) luminescence (F), while high sulfur regions exhibit dark luminescence (F).

to the published data. The crust-normalized concentrations of all plotted elements overlap the field for igneous magnetite except for Si, Ca, Y, P, and Ge that are elevated in some samples, and Al, Ga, Mn, Ti, and Zn that are slightly depleted in some samples relative to published data. As expected, the geochemical data for surface samples from Cristales Grandes, Rodados Negros, and San Vicente Alto, and surface and drill core samples from Laco Sur and Laco Norte overlap the signature for magnetite from Kiruna-type deposits. The continental-crust-normalized concentrations of Zr, Hf, and Ge determined in the present study are elevated relative to data

reported by Dare et al. (2014), whereas the concentration of Ga in samples from San Vicente Alto is slightly lower than that reported by those authors. The overlap between the trace element chemistry of magnetite from surface and drill core samples reported in this study and magmatic-hydrothermal magnetite and magmatic magnetite suggests that magmatic and high-temperature hydrothermal fluids played a role in the genesis of the El Laco orebodies.

The [Al + Mn] and [Ti + V] data for magnetite from the five orebodies investigated are compared in Figure 6 with data for magnetite from the andesite host rocks (cf. Dare et al., 2015)

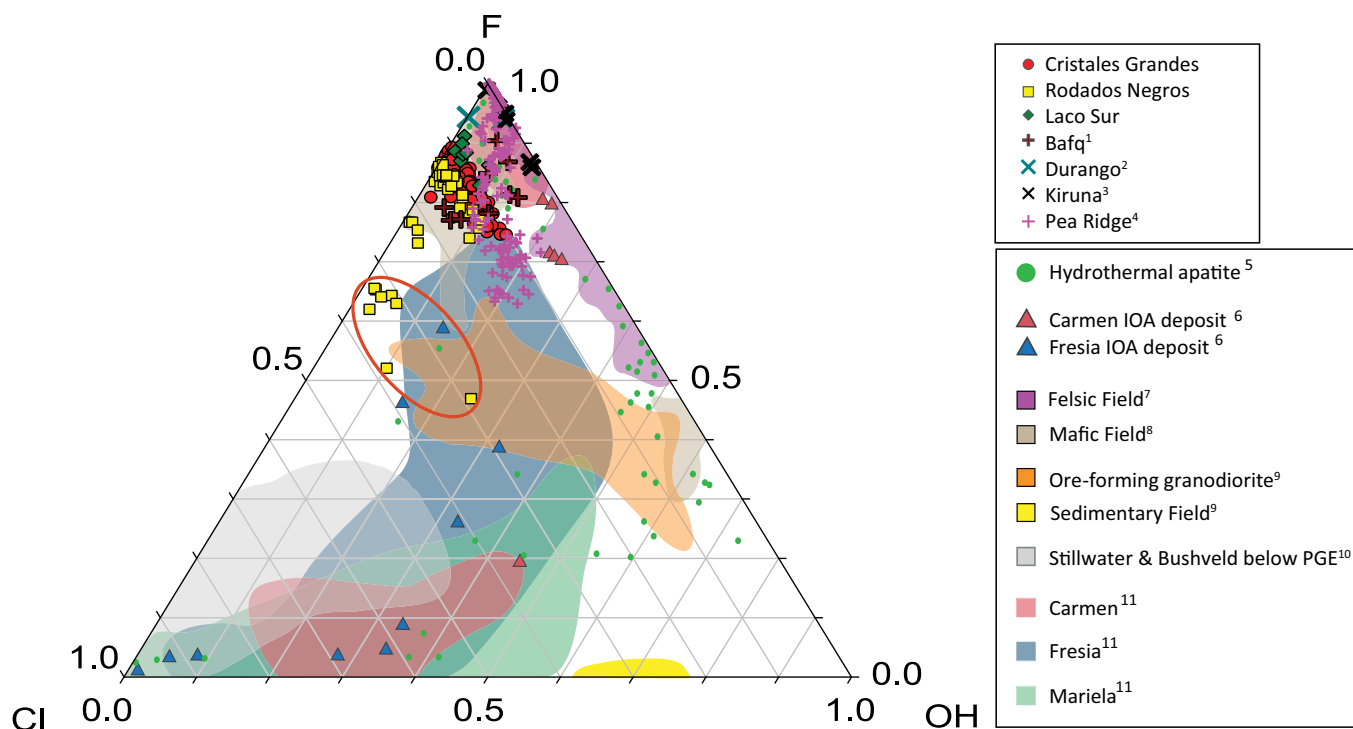


Fig. 8. Comparison of F-Cl-OH compositions of apatite from Cristales Grandes, Rodados Negros, and Laco Sur with compositions of apatite from IOA deposits, e.g., Cerro de Mercado (Durango) Carmen, Fresia, and Pea Ridge, and those in the Kiruna and Bafq districts, mafic, felsic, and intermediate rocks, hydrothermal and sedimentary environments, and below the PGE ore zones at the Stillwater and Bushveld Complexes. The apatite at El Laco is fluorapatite and has composition similar to primary apatite in Cretaceous IOA deposits from the Chilean iron belt and IOA deposits globally. The apatite chemistry is consistent with growth from magmatic and magmatic-hydrothermal fluids. Comparison data obtained from ¹Torab and Lehman (2007); ²Marks et al. (2012); ³Harlov et al. (2002); ⁴Harlov et al. (2016); ⁵Webster and Piccoli (2015); ⁶Treloar and Colley (1996); ⁷Barth and Dorais (2000), Belousova et al. (2002), Krneta et al. (2016); ⁸Marks et al. (2012), Patiño Douce et al. (2011); ⁹Bao et al. (2016); ¹⁰Boudreau et al. (1995); ¹¹Palma et al. (2019). The orange ellipse highlights chlorine-enriched apatite from Rodados Negros (yellow squares), which has porous texture and contains monazite inclusions (Fig. 7C, D).

and magnetite from a variety of different ore forming environments (Nadoll et al., 2014). The compositions of magnetite from Cristales Grandes, Rodados Negros, and the shallow massive magnetite body at Laco Sur plot in the Kiruna field (Fig. 6A). The compositions of magnetite from surface samples of all five orebodies plot in the IOCG field (Fig. 6A). The compositions of magnetite from surface samples at Rodados Negros, Laco Sur, and Laco Norte plot in the BIF field, and a few data for magnetite from Cristales Grandes, Rodados Negros, and the deep samples at Laco Sur and Laco Norte plot in the skarn field. The compositions of magnetite from the deep levels of Laco Norte and the deep and intermediate levels of Laco Sur (Fig. 6B) plot in the igneous Fe-Ti/V field, and some samples from Laco Sur have [Ti + V] contents that overlap magnetite from the El Laco andesite host rocks (Fig. 6B). Compositional data for magnetite from Cristales Grandes, Rodados Negros, intermediate depths of Laco Norte, and all depths of Laco Sur plot in the porphyry field (Fig. 6B). The observation that compositional data for magnetite from the El Laco orebodies plot in all fields in the magnetite discriminant diagram indicates that the diagram is not able to distinguish magnetite from different ore deposit types; however, as discussed below, using the temperature-composition data from Nadoll et al. (2014) places constraints on the temperature of

crystallization of magnetite as a function of depth in the El Laco orebodies.

However, the comparisons in Figure 6 reveal differences of [Al + Mn] and [Ti + V] content among different orebodies at El Laco, as well as systematic decreases of these elements among samples within individual orebodies that can be used to infer differences in temperature of crystallization within and among the orebodies. The compositions of magnetite from the dike-like orebodies at Cristales Grandes and Rodados Negros and from the flow-like orebodies (San Vicente Alto, Laco Sur, and Laco Norte) record crystallization at temperatures >500°C, 300 to 500°C, and 200 to 300°C, respectively (Fig. 6; Nadoll et al., 2014). The temperatures inferred from magnetite chemistry for Rodados Negros are consistent with homogenization temperatures of fluid inclusions hosted in apatite from that orebody (cf. Broman et al., 1999). Overall, the considerable overlap for all samples in [Al + Mn] and [Ti + V] space is consistent with magnetite that grew from a cooling magmatic-hydrothermal fluid.

In Figure 9, the vanadium and titanium contents of magnetite grains from the orebodies and andesite host (cf. Broughm et al., 2017) at El Laco and the Láscar dacite (cf. Broughm et al., 2017) are plotted along with fields that define the range of vanadium and titanium in magnetite from magmatic and

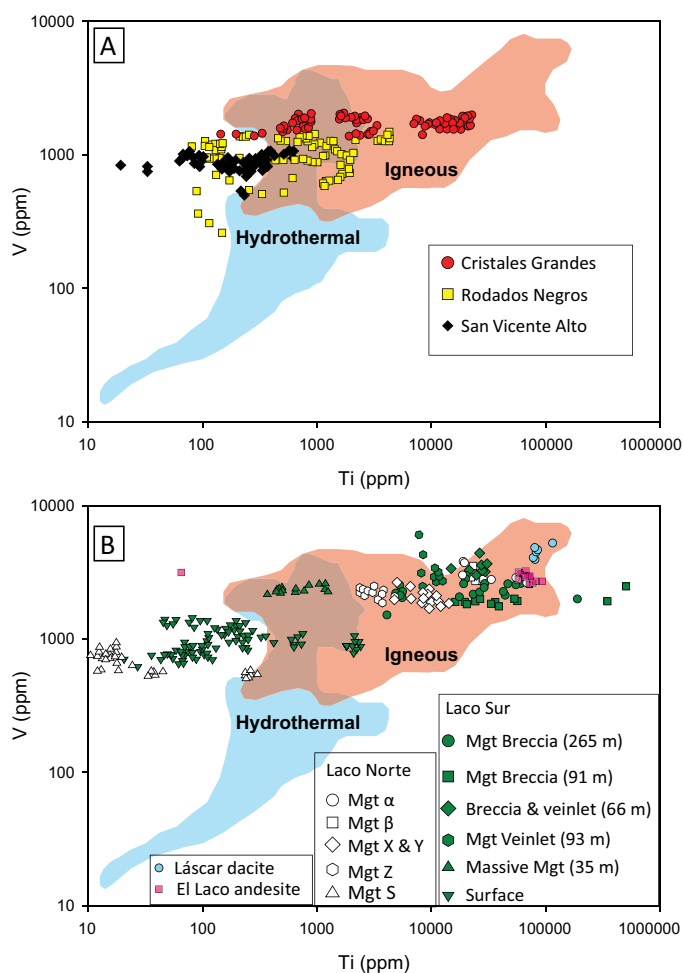


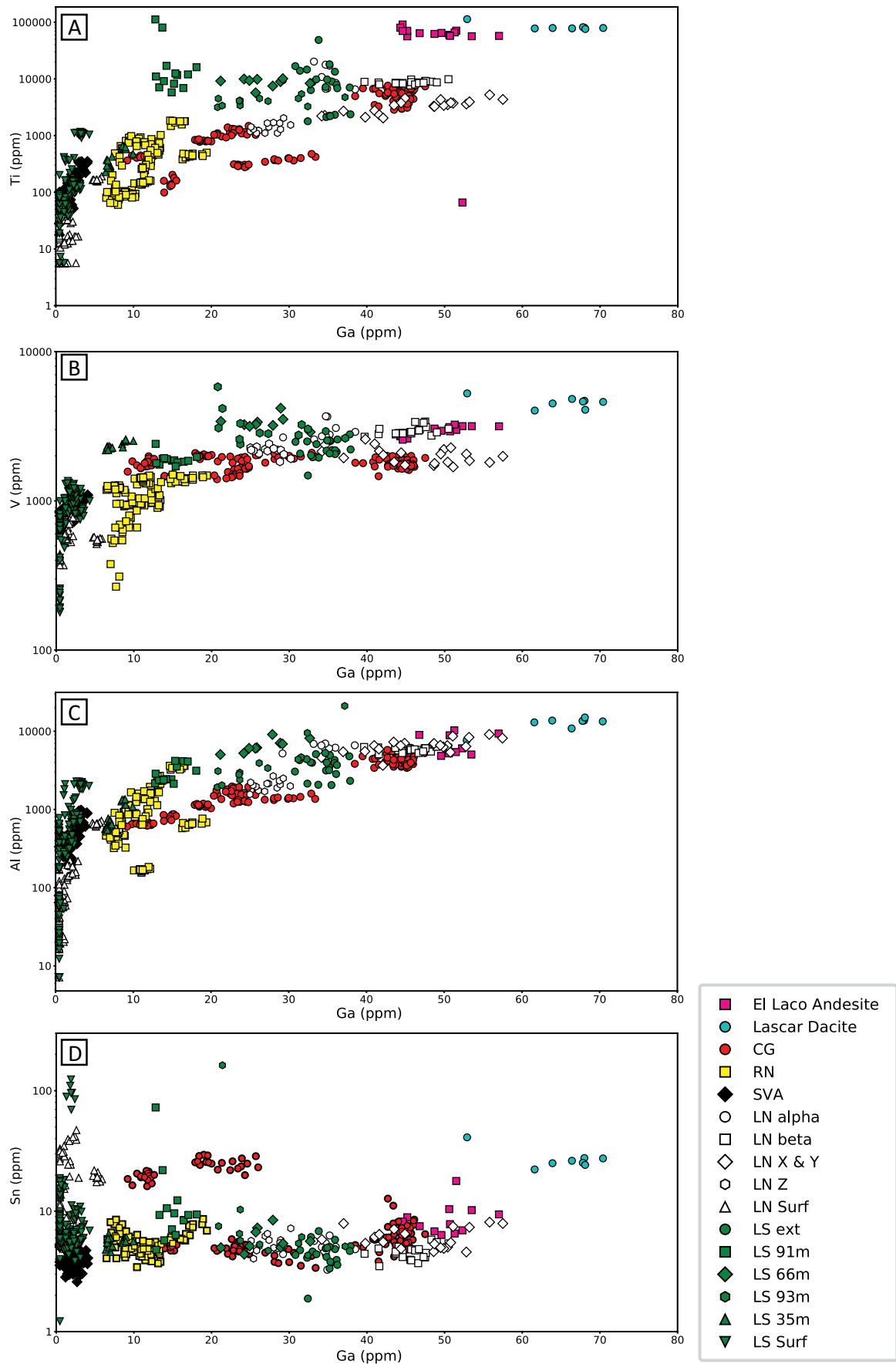
Fig. 9. Comparison of vanadium and titanium contents of magnetite from surface (A) and drill core (B) from the El Laco orebodies, the El Laco andesite, and Láscar dacite (cf. Broughm et al., 2017) with fields for vanadium and titanium content for magnetite from igneous and hydrothermal environments (cf. Dare et al., 2014, and Knipping et al., 2015b). Magnetite from Cristales Grandes, Rodados Negros, and deep to intermediate levels of the orebodies at Laco Sur and Laco Norte plot in the composition field seen in igneous magnetite, whereas data for magnetite from Cristales Grandes, Rodados Negros, San Vicente Alto, and the shallow levels of the orebodies at Laco Sur and Laco Norte plot in the region where the fields for hydrothermal and igneous magnetite overlap. A few data points from San Vicente Alto plot in the field for hydrothermal magnetite and data from all surface samples studied plot in the low-titanium region of the field. These data are consistent with growth of magnetite from magmatic and magmatic-hydrothermal fluids.

hydrothermal environments (cf. Dare et al., 2014; Knipping et al., 2015b). Vanadium content is controlled by oxygen fugacity, while the titanium content of magnetite is strongly controlled by temperature (Lindsley, 1991; Nielsen et al.,

1994; Toplis and Carroll, 1995; Balan et al., 2006; Bordage et al., 2011). Nadoll et al. (2014) showed that the concentrations of both vanadium and titanium in magnetite decrease with decreasing magnetite crystallization temperature. The vanadium and titanium contents of magnetite from deep and intermediate depths at Laco Sur and Laco Norte, in addition to data for some surface samples from Cristales Grandes and Rodados Negros, plot in the field for igneous magnetite (Fig. 9). The vanadium and titanium contents of surface samples from Cristales Grandes, Rodados Negros, San Vicente Alto, Laco Norte, and Laco Sur, in addition to data for massive magnetite collected 35 m below surface at Laco Sur, plot in the area where the igneous and hydrothermal fields overlap (Fig. 9). A few data points for magnetite from San Vicente Alto plot in the field for hydrothermal magnetite, and some data from surface samples from all orebodies plot outside the fields in the low titanium region of the plot (Fig. 9). The distribution of data for samples from the five orebodies is similar to that reported by Broughm et al. (2017) who found an almost identical spread of vanadium and titanium concentrations at El Laco. Notably, the data reported here demonstrate that magnetite in the deeper levels of Laco Sur, Extensión Laco Sur, and Laco Norte has titanium concentrations that overlap those for igneous magnetite from the El Laco andesite host and nearby Láscar dacite (Fig. 9B; Broughm et al., 2017).

Nadoll et al. (2014) reported that Ti, V, Al, Sn, and Ga concentrations are highest in igneous magnetite and decrease systematically in magnetite that forms in hydrothermal systems as a function of decreasing temperature. Salazar et al. (2019) also reported that the vanadium and gallium concentrations in magnetite from the Cerro Negro Norte IOA deposit in the Chilean iron belt display a cooling trend from magmatic to hydrothermal conditions. In Figure 10, the concentrations of Ti, V, Al, and Sn are each plotted against Ga. The data for the El Laco orebodies indicate decreasing Ti, V, Al, and Ga concentrations in surface samples from Cristales Grandes, to Rodados Negros, to San Vicente Alto (Fig. 10). The concentrations of gallium in drill core samples from Laco Sur and Laco Norte decrease from depth to surface, while the tin concentrations have an average value of ~10 ppm (Fig. 10D). However, a subset of the data for the surface samples from Laco Norte and Laco Sur, and deep drill core samples from Laco Sur has increased tin content similar to that observed in hydrothermal magnetite from the Mg skarn ore at the Santa Rita deposit and in igneous magnetite from the Henderson Climax-type Mo deposit as reported by Nadoll et al. (2014). Those authors suggested that the high tin contents of magnetite from Santa Rita and Henderson are controlled by fluid composition during fluid-host rock interactions. The high tin content in the magnetite at Laco Sur and Laco Norte is, therefore, either the result of ore fluid composition or fluid-rock interactions.

Fig. 10. Comparison of (A) Ti, (B) V, (C) Al, (D) Sn, versus Ga contents in magnetite from surface and drill core from the El Laco orebodies, the El Laco andesite host rocks, and Láscar dacite (cf. Broughm et al., 2017). Igneous magnetite from the El Laco andesite host rocks and Láscar dacite have higher Ti, V, Al, and Ga contents. Generally, Ti, V, and Al contents decrease from deep to shallow regions in the deposit. Overall, there is a decrease in the tin content of magnetite from Cristales Grandes, to Rodados Negros to San Vicente Alto for the surface samples. For drill core samples, the tin content is highest in surface samples from Laco Sur but there are also two analyses of magnetite from deep breccias that have similarly high Sn contents. The surface samples from both Laco Norte and Laco Sur have higher tin contents than the shallow, intermediate, and deep portions of these orebodies.



Further, magnetite with high Sn content (~100 ppm) at Laco Sur also contains the highest concentrations of Nb (average value of ~580 ppm), Th (~455 ppm), and U (~253 ppm), as well as Nb-rich oxide inclusions in the magnetite grains. We hypothesize that the high Sn (and Nb) concentrations with corresponding low Ga concentrations reflect metasomatic alteration after ore emplacement, since these magnetite grains also contain elevated levels of Th, U, and REEs, which can be liberated during metasomatic reactions with apatite and hydrothermal fluids (Harlov et al., 2002). The trace element concentrations in magnetite from the El Laco orebodies are consistent with growth of magnetite from a cooling magmatic-hydrothermal fluid as it ascended through the crust.

Wen et al. (2017) proposed a new plot for discriminating between magmatic and hydrothermal magnetite that considers the hydrothermal reequilibration of igneous magnetite. Wen et al. (2017) found that plotting the V/Ti ratio versus the Fe content of magnetite allows for the discrimination of magmatic magnetite, magmatic magnetite that has reequilibrated with a hydrothermal fluid, and purely hydrothermal magnetite. In Figure 11, we compare our data for magnetite from the five orebodies and host andesite (Dare et al., 2015) at El Laco, the discriminant fields of Wen et al. (2017) (lines), and (colored) fields representing igneous, magmatic-hydrothermal, and low-temperature hydrothermal magnetite based on data from Nadoll et al. (2014). Data for magnetite from surface samples from all orebodies, and from the deep, intermediate, and shallow zones of the drill cores plot in the field for reequilibrated magnetite. Data from all surface samples and all levels of the drill cores plot in the field for hydrothermal magnetite defined by Wen et al. (2017). The vast majority of the data from the El Laco orebodies plot in the overlapping region of the fields for igneous and magmatic-hydrothermal magnetite from Nadoll et al. (2014) that we superposed in the Wen et al. (2017) plot. The deepest samples from the drill cores plot in the field for igneous magnetite from Nadoll et al. (2014), and no data plot in the field for low-temperature hydrothermal magnetite. Similar to Wen et al. (2017), we observe textural and chemical evidence for reequilibration of igneous magnetite with magmatic-hydrothermal fluid, and growth of magnetite from magmatic-hydrothermal fluids. Magnetite at depth in drill core contains ilmenite exsolution lamellae surrounded by magnetite with no exsolution lamellae (Fig. 2I) or inclusion-rich magnetite cores surrounded by inclusion-poor rims (Fig. 2J). Magnetite grains from surface samples terminate at triple junctions (Figs. 2H, I), consistent with reequilibration of magnetite with magmatic-hydrothermal fluid. Overall, the compositions of magnetite from El Laco plotted in the V/Ti vs. Fe diagram of Wen et al. (2017), with the fields for data from Nadoll et al. (2014), are consistent with magmatic-hydrothermal fluids being responsible for formation of the orebodies.

Insights for ore-forming processes from El Laco apatite chemistry

Apatite ($\text{Ca}_{10}(\text{PO}_4)_6(\text{F,Cl,OH})_2$) is a common accessory mineral in many terrestrial and extraterrestrial geologic environments. Apatite is able to incorporate nearly one-third of the elements in the periodic table into its structure, including the essential

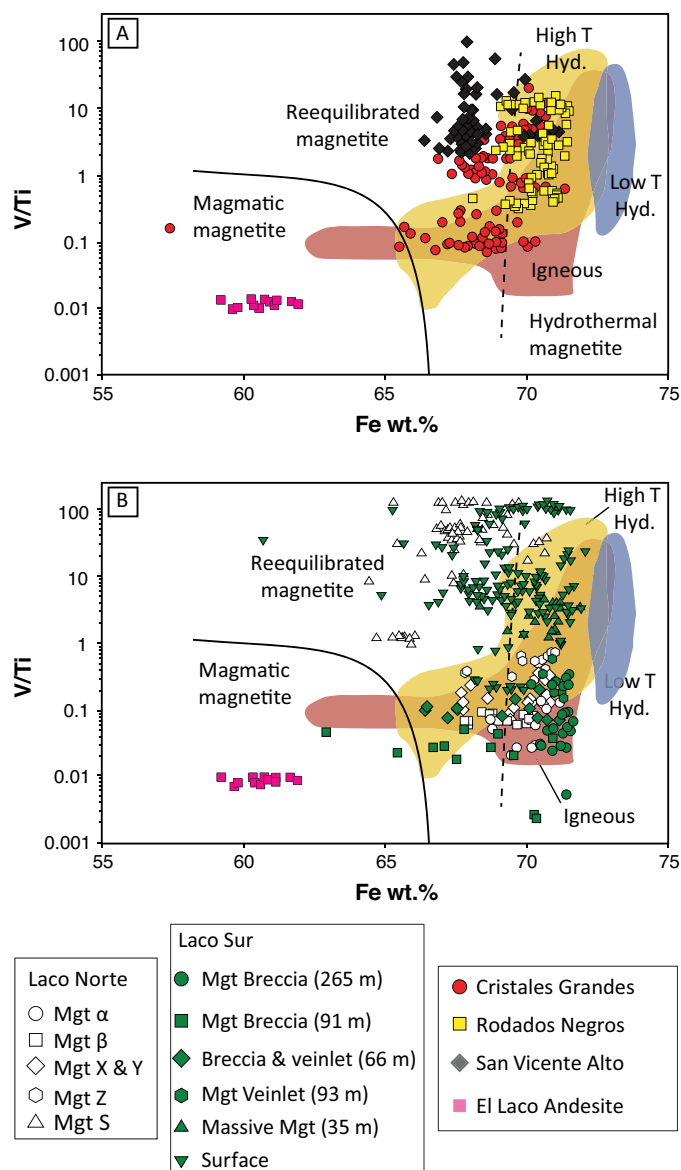


Fig. 11. Comparison of V/Ti and Fe content of magnetite (Mgt) from surface outcrops (A) and drill core (B) from the El Laco orebodies, and the El Laco andesite (cf. Dare et al., 2015) with the fields for magmatic, reequilibrated, and hydrothermal magnetite (cf. Wen et al., 2017), and colored fields for igneous, high- and low-temperature hydrothermal magnetite (cf. Nadoll et al., 2014). The comparison indicates growth of magnetite in the orebodies from magmatic and magmatic-hydrothermal fluids and is consistent with ore genesis at El Laco according to the model presented by Ovalle et al. (2018).

structural constituents F, OH, and Cl, as well as trace elements such as S, REEs, and Fe (Hughes and Rakovan, 2015). Trace element abundances in apatite have been used as petrogenetic indicators to gain insights into the evolution of geologic systems (Streck and Dilles, 1998; Belousova et al., 2002; Piccoli and Candela, 2002; Parat et al., 2011; Harlov, 2015; Hughes and Rakovan, 2015; Webster and Piccoli, 2015; Bouzari et al., 2016; Mao et al., 2016; Konecke et al., 2017a, b).

Generally, the apatite grains from Laco Sur, Cristales Grandes, and Rodados Negros are fluorapatite with lesser amounts of Cl and OH (Fig. 8). Our data are consistent with

Dare et al. (2015) who reported that apatite contains, on average, ~2 wt % F. The analyses of some fluorapatite grains from Laco Sur yielded fluorine concentrations greater than the stoichiometric concentration for pure, end-member fluorapatite (3.77 wt %). This is not an analytical artifact considering the reproducibility of the standards (Schettler et al., 2011) and strict adherence to the analytical protocol of Stromer et al. (1993) and Goldoff et al. (2012). We highlight that high F concentrations (>3.77 wt %) have also been reported for fluorapatite from Kiruna-type deposits in the Kiruna and Grängesberg districts in Sweden and the Pea Ridge IOA deposit, United States (Fig. 8; Harlov et al., 2002, 2016; Jonsson et al., 2016). Fluorapatite from Laco Sur, Cristales Grandes, and Rodados Negros cluster near the fluorine end of the F-Cl join and overlap with apatite compositions from mafic igneous rocks and their evolved ore deposits (Marks et al., 2012; Rojas et al., 2018).

The El Laco fluorapatite data overlap data for apatite from other IOA deposits, including Pea Ridge (United States), Cerro de Mercado (Durango, Mexico), deposits in the Bafq (Iran), Kiruna (Sweden), and Grängesberg (Sweden) districts, the Carmen deposit in the Chilean iron belt, the Great Bear magmatic zone, and hydrothermal apatite, which also plot near the fluorine apex of the ternary (Fig. 8; Harlov et al., 2002, 2016; Torab and Lehman, 2007; Marks et al., 2012; Taghipour et al., 2015; Jonsson et al., 2016; Mao et al., 2016; Normandeau et al., 2018; Palma et al., 2019). The chlor-fluorapatite grains from Rodados Negros (highlighted by the orange ellipse in Fig. 8) have increased chlorine content and are shifted toward the chlorine end of the F-Cl join, consistent with halogen chemistry reported for apatite from the Los Colorados (La Cruz et al., 2019) and Fresia IOA deposits (Palma et al., 2019) in the Chilean iron belt. Broman et al. (1999) reported that apatite-hosted fluid inclusions from Rodados Negros contain up to 60 wt % NaCl equiv, thus the chlorine enrichment in grains from Rodados Negros most likely reflect growth from, or reequilibration with, this Cl-rich, F-poor fluid. The composition of apatite from hydrothermal environments exhibits a wide range of F, Cl, and OH concentrations that reflect the composition of the hydrothermal fluid from which apatite precipitates, the temperature of mineralization, and the preference for the anions ($F \gg Cl > OH$) in the apatite structure (cf. Boudreau et al., 1995; Barth and Dorais, 2000; Belousova et al., 2002; Patiño Douce et al., 2011; Marks et al., 2012; Hughes and Rakovan, 2015; Webster and Piccoli, 2015; Bao et al., 2016; Krneta et al., 2016). The majority of analyzed apatite grains from El Laco are compositionally similar to fluorapatite from mafic igneous rocks and hydrothermal fluids evolved from mafic silicate melts and are consistent with growth from a silicate melt or magmatic-hydrothermal fluid.

The Cl-enriched domains in some apatite grains from Rodados Negros are consistent with the variability of cathodoluminescence (CL) in those apatite grains and variations in the concentrations of CL activators such as Ce^{3+} , Eu^{2+} , and Mn^{2+} , and quenchers such as Fe^{2+} and La^{3+} (cf. Kempe and Götz, 2002). The areas of bright luminescence in apatite grains from Rodados Negros have the highest chlorine content of all apatite grains from the El Laco orebodies and correspond spatially to the porous/mottled regions of those apatite grains.

The areas of dark luminescence in fluorapatite from Laco Sur have the highest sulfur content (up to ~1 wt % S) among all apatite grains from the El Laco orebodies. Sulfur, Cl, Mn, REEs, and Fe are highly mobile in magmatic-hydrothermal fluids (Hedenquist and Lowenstern, 1994; Reed et al., 2000; Williams-Jones and Heinrich, 2005; Simon et al., 2007; Simon and Ripley, 2011). The enrichment of these elements within the apatite grains, in addition to the presence of monazite inclusions within and between grains, is consistent with late-stage reequilibration of the apatite with mineralizing magmatic-hydrothermal fluids.

Magnetite- and apatite-hosted mineral inclusions

The presence of mineral inclusions in magnetite (e.g., monazite, apatite, thorite, and Nb-rich oxide; Fig. 2) and apatite (e.g., monazite; Fig. 7B) from the El Laco orebodies has not, to our knowledge, been reported in previous studies for this deposit. Monazite and thorite inclusions in apatite have been reported from IOA deposits in the Chilean iron belt in northern Chile (La Cruz et al. 2019; Palma et al., 2019), the Kiruna, Grängesberg, and Bafq districts (Harlov et al., 2002; Bonyadi et al., 2011; Jonsson et al., 2016), and the Olympic Dam IOCG deposit in Australia (Krneta et al., 2016). Inclusions of monazite have been identified in the banded iron ore at Kiirunavaara, and intergrown with the iron oxides and apatite in the magnetite and hematite zones in the Pea Ridge deposit (Harlov et al., 2002, 2016). Many authors explain the presence of these inclusions in apatite as the result of metasomatic alteration of apatite (Harlov et al., 2002, 2016; Bonyadi et al., 2011; Krneta et al., 2016; Palma et al., 2019; Sadove et al., 2019). For instance, Palma et al. (2019) reported that altered Cl-OH apatite from the Carmen and Fresia IOA deposits in the Chilean iron belt contains inclusions of monazite and xenotime and proposed that the inclusions record fluid-induced dissolution-reprecipitation of apatite during metasomatism. Alternatively, monazite and thorite inclusions in magnetite samples may reflect growth of those phases as a result of local supersaturation of REE, Th, Si, and P in the fluid in contact with the magnetite grains (La Cruz et al., 2019).

The presence of the Nb-rich oxides, which were observed along cracks between magnetite S2 and high Si and Mg magnetite A (Fig. 2F), and monazite inclusions in magnetite from Laco Sur (Fig. 2D), although not reported by Dare et al. (2015) and Broughm (2017), is consistent with the high field strength element (HFSE) and light rare earth element (LREE) magnetite signatures reported by those authors. Magnetite grains that host Nb-rich oxides are depleted in Nb as well as Ti, Al, V, and Mn. This observation is consistent with the growth of Nb oxide during hydrothermal alteration of originally Nb-enriched magnetite by meteoric fluids (Giovannini et al., 2017), which is supported by the hydrogen and oxygen stable isotope signatures of these magnetite grains (Childress et al., 2020).

Postmineralization alteration of the orebodies

Goethite and hematite in surface samples from San Vicente Alto, Laco Sur, and Laco Norte indicate oxidation and hydration of magnetite, which Alva-Valdivia et al. (2003) reported can occur by supergene alteration. Those authors report that the greater degree of oxidation observed in samples from Laco Norte reflects greater degrees of alteration by meteoric

waters relative to samples from Laco Sur that exhibit less oxidation. It is well established that goethite is a product of the oxidation and low-temperature hydrothermal alteration of titanomagnetite (Alt and Honnorez, 1984; Xu et al., 1997). Childress et al. (2020) present O (^{16}O , ^{17}O , and ^{18}O) and H stable isotope data and H_2O contents of aliquots of the same surface samples investigated in this study. Values of $\delta^2\text{H}$ reported by Childress et al. (2020) become increasingly negative with increasing H_2O contents, and $\Delta^{17}\text{O}$ and $\delta^{18}\text{O}$ values fingerprint low- and high-altitude meteoric water in samples with increasing goethite contents. Thus, we conclude that goethite, and possibly hematite, formed by secondary processes after emplacement of the orebodies.

Formation of the El Laco orebodies

The body of data presented here for magnetite and apatite geochemistry is most consistent with formation of the El Laco orebodies by a combination of igneous and magmatic-hydrothermal processes. The data support the new genetic model for El Laco proposed by Ovalle et al. (2018). Here, we briefly summarize that model, which is based on the magnetite flotation model of Knipping et al. (2015a, 2019). The trace element-rich magnetite in the deeper levels of the orebodies crystallized from silicate melt, wherein magnetite is the liquidus and only crystalline phase in oxidized, water-rich andesitic melt over a large range of pressure and temperature space (Martel et al., 1999; Knipping et al., 2019). After crystallization of magnetite, decompression of the silicate melt causes it to reach volatile saturation and exsolve a magmatic-hydrothermal fluid. Magnetite nanolites and microlites serve as nucleation surfaces for magmatic-hydrothermal fluid as it exsolves from silicate melts, a process that has been demonstrated experimentally (Hurwitz and Navon, 1994; Knipping et al., 2019; Pleše et al., 2019) and numerically (Edmonds et al., 2014). Continued degassing of the silicate melt during magma decompression results in the formation of a magnetite-fluid suspension that is less dense than the surrounding magma (Gualda and Ghiorso, 2007; Edmonds et al., 2014; Ovalle et al., 2018; Knipping et al., 2019). The magmatic-hydrothermal fluid component of the suspension would be chlorine and iron rich, based on experiments that demonstrate the efficient partitioning of these elements from silicate melt to exsolved aqueous fluid (Simon et al., 2004; Bell and Simon, 2011; Audétat and Simon, 2012). This is consistent with fluid inclusion studies of samples from El Laco that document the high-temperature chlorine-rich nature of the mineralizing fluid at El Laco (Broman et al., 1999). The experimental results of Knipping et al. (2019) demonstrate that the wettability of magnetite is enhanced with increasing chlorine concentration of the magmatic-hydrothermal fluid and that the diameter of magnetite grains that crystallize from silicate melt decreases with increasing chlorine content of the melt. Thus, a smaller average magnetite crystal diameter makes the formation of a magnetite-fluid suspension more efficient. The magmatic-hydrothermal fluid also scavenges elements such as F, P, and Ca that allow the precipitation of fluorapatite in the orebodies.

During the collapse of the volcanic edifice at El Laco, as evidenced by the observation of fissures and ring structures (Ovalle et al., 2018), the magnetite-fluid suspension was

forcibly injected into the upper crust where it formed the hydrothermal breccia bodies observed in drill core from the deeper levels of the deposit. The observation that magnetite grains with ilmenite oxyexsolution lamellae (Fig. 2) are only found at intermediate to deeper levels of the orebody plausibly reflects gravitational settling during ascent of originally igneous titanomagnetite grains, which were swept up by the exsolving magmatic-hydrothermal fluid that nucleated on those grains in the parent silicate melt. As discussed in Knipping et al. (2015a), the presence of magnetite nanolites and microlites in the magnetite-fluid suspension significantly increases the total mass of iron that can be advected from the source magma into the overlying crust. Continued ascent, shallow-level emplacement, and surface venting of the magnetite-fluid suspension gave rise to the formation of the massive magnetite flows and dike-like bodies that outcrop around the Pico Laco resurgent dome. Hydrothermal magnetite that grows from the iron-rich magmatic-hydrothermal fluid component of the magnetite-fluid suspension in the upper portions of the orebodies should be progressively depleted in minor and trace elements from the deeper levels of the orebodies to the surface considering the expected vertical thermal gradient; this is consistent with the data reported here. As discussed by Ovalle et al. (2018), empirical studies of industrial froth flotation processes indicate that a magnetite-fluid suspension will have rheological properties similar to basaltic lava flows, which explains the presence of cavities and gas escape tubes in surface outcrops originally described by Park (1961). A comparison of the textures of samples from El Laco with textures produced during industrial froth flotation reveals remarkable similarities (Fig. 12), consistent with formation of the El Laco orebodies by shallow emplacement and venting of a magnetite-fluid suspension. The presence of triple junctions among magnetite grains at El Laco plausibly reflects equilibration of magnetite with interstitial high-temperature ore fluid during or after emplacement, which also explains the presence of monazite, thorite, and Nb oxide inclusions in magnetite, monazite inclusions in apatite, and magnetite octahedra observed growing from the walls of cavities and gas escape tubes. Circulation and cooling of the interstitial magmatic-hydrothermal fluid also explains the presence of sulfide-bearing magnetite-diopside-scapolite veins and late veinlets of gypsum-magnetite-pyrite that crosscut the main breccia bodies at depth (Ovalle et al., 2018), as well as the advanced argillic alteration at the surface (Sillitoe and Burrows, 2002).

The El Laco orebodies contain ~367 Mt of iron, based on the reported resources of ~734 Mt at an average grade of ~49% iron (CAP Minería, 2014). Following the methodology of Knipping et al. (2015a), if the magnetite-fluid suspension evolved from a hydrous magma that contained 6 wt % H_2O , and the suspension contained 20 wt % primary titanomagnetite, a parent magma on the order of 50 km^3 is required to account for the iron in the El Laco orebodies if 50% of the iron in the fluid phase, carried as FeCl_2 , precipitated during emplacement. This magma volume is consistent with typical arc volcano magma chambers ($4\text{--}60 \text{ km}^3$; Marsh, 1989) and seems plausible considering the $\sim 30\text{-km}^2$ diameter area that contains the orebodies at El Laco (Oyarzún and Frutos, 1984; Nyström and Henríquez, 1994).

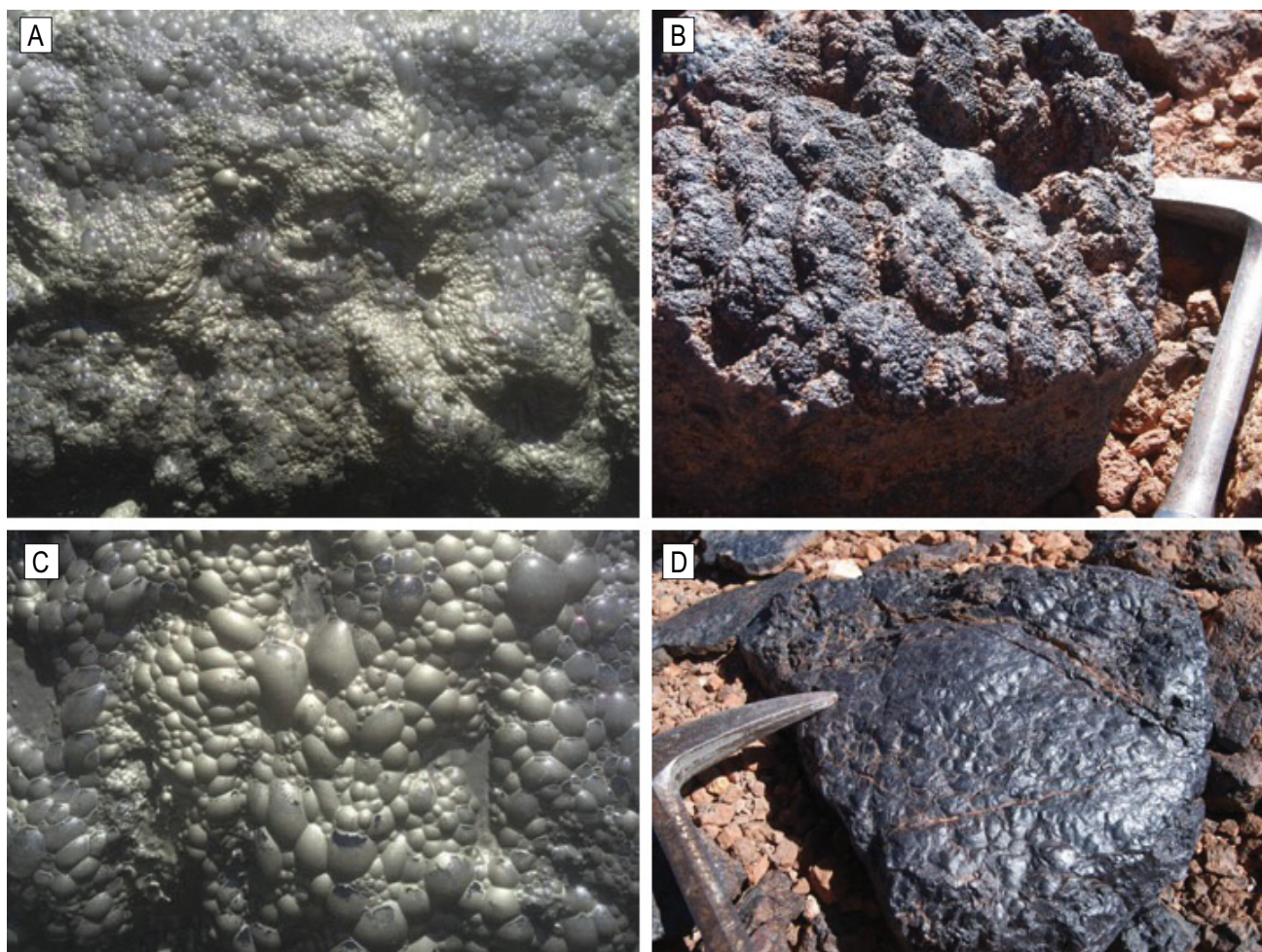


Fig. 12. Comparison of the textures produced during industrial froth flotation (A, C) and magnetite ore at the El Laco deposit (B, D).

Finally, we highlight that the $\delta^{18}\text{O}$, $\Delta^{17}\text{O}$, $\delta^2\text{H}$, and $\delta^{56}\text{Fe}$ data reported by Childress et al. (2020) and Bilenker et al. (2016) are consistent with the model presented here for the formation of the El Laco orebodies. Childress et al. (2020) report $\delta^{56}\text{Fe}$ and $\delta^{18}\text{O}$ values for magnetite from outcrop samples collected from Cristales Grandes, Laco Norte, Laco Sur, Rodados Negros, and San Vicente Alto, which in addition to the magnetite geochemistry presented here for the same samples, are consistent with magnetite crystallization from magmatic-hydrothermal fluid and/or silicate melt. They report that values of $\delta^2\text{H}$ become increasingly negative with increasing goethite modal abundance and H_2O content of the samples. The $\Delta^{17}\text{O}$, which is defined as $\delta^{17}\text{O}_{\text{sample}} - \delta^{18}\text{O}_{\text{sample}} \times 5.302$, and $\delta^{18}\text{O}$ data for goethite-bearing samples indicate alteration of primary magmatic and magmatic-hydrothermal magnetite by meteoric water. Importantly, the oxygen isotope data for samples from the El Laco orebodies disallow formation by liquid immiscibility based on the experimental data of Lester et al. (2013a) that constrain the partitioning of O isotopes between conjugate Fe- and Si-rich melts. Lester et al. (2013a) reported values of $\Delta^{18}\text{O}$, which is defined as $\delta^{18}\text{O}_{\text{Si-rich melt}} - \delta^{18}\text{O}_{\text{Fe-rich melt}}$, of 0.5 to 0.6‰, requiring that the Fe oxide orebodies at El Laco should yield $\delta^{18}\text{O}$ values of ~7 to 9‰ if they crystallized from

an iron-rich liquid that had been in equilibrium with andesite host rocks. Rather, the El Laco orebodies yield $\delta^{18}\text{O}$ values of ~3.5 to 5‰ and the andesite host rock yield $\delta^{18}\text{O}$ values of ~8 to 9‰, eliminating the possibility that silicate magmas in the El Laco plumbing system could be related to magnetite in the orebodies by liquid immiscibility. The $\delta^{18}\text{O}$ values of ore samples from El Laco match exactly the values expected for magnetite precipitated from a magmatic-hydrothermal fluid. The constraints from oxygen isotope data are also consistent with experimental data from Lester et al. (2013b) that demonstrate that liquid immiscibility does not occur in $\text{H}_2\text{O} + \text{Cl}$ -bearing silicate melts because the presence of chlorine increases the activity of silicon in the melt, resulting in increased temperatures for the silicate mineral saturation surface, and eliminates unmixing of the silicate liquid. The chlorine-rich nature of the ore fluids at El Laco as demonstrated by Broman et al. (1999), coupled with the experimental and oxygen isotope partitioning results of Lester et al. (2013a, b) falsify the liquid immiscibility hypothesis.

Conclusions

Magnetite from five orebodies and apatite from three orebodies at the El Laco iron oxide-apatite deposit in Chile have

major, minor, and trace element chemistry consistent with growth from both a silicate melt and a magmatic-hydrothermal fluid. Our data for magnetite from the El Laco iron oxide-apatite orebodies plot in multiple fields on the [Al + Mn] versus [Ti + V] discriminant diagram of Nadoll et al. (2014); this indicates that this diagram is more suitable for identifying the temperature of crystallization of magnetite rather than the type of ore deposit from which magnetite is sourced. Magnetite grains from El Laco contain mineral inclusions that preserve evidence of reequilibration of ore minerals with hydrothermal fluids during or after emplacement of the orebodies. These observations are consistent with ore genesis at El Laco via shallow-level emplacement and surface venting of magnetite-bearing magmatic-hydrothermal fluid suspensions according to the model described in Ovalle et al. (2018). The current study adds to a growing body of geochemical and petrographic data for ore minerals from IOA deposits that indicate formation of Kiruna-type IOA deposits via the ascent of a cooling, decompressing Fe-bearing magmatic-hydrothermal fluid that contains and transports igneous titanium-rich magnetite nanolites and microlites.

Acknowledgments

NLL and TMC acknowledge the Society of Economic Geologists Foundation (SEGf) for funding via the Student Research Grant program (2016), and field trip funding to the University of Michigan SEG Student Chapter via the Steward R. Wallace fund, which allowed for field work and sample collection at El Laco. JTO acknowledges the SEGf for funding via the Graduate Student Fellowship Program (2017). ACS thanks the NSF for funding under grants EAR 1924142, and 1524394. MR and FB recognize and acknowledge the Millennium Science Initiative (via the Millennium Nucleus for Metal Tracing along Subduction grant NC130065), FONDECYT (grant 1140780), and FONDAP (project 15090013: Centro de Excelencia en Geotermia de Los Andes) for funding. We thank Mario Rojo and Alejandro Mardones from Compañía Minera del Pacífico for access to the deposit for sample collection. We thank Dale “Mr. Wizard” Austin for his assistance making the figures in the manuscript. We thank Steve Kesler for providing feedback which greatly improved the manuscript prior to submission. We thank Larry Meinert for the editorial handling of this manuscript, and we thank Warren Day, Dan Harlov, and Associate Editor Murray Hitzman for their thorough and thoughtful reviews, which greatly improved the manuscript.

REFERENCES

- Alt, J.C., and Honnorez, J., 1984, Alteration of the upper oceanic crust, DSDP site 417: Mineralogy and chemistry: Contributions to Mineralogy and Petrology, v. 87, p. 149–169.
- Alva-Valdivia, L.M., Rivas, M.L., Gognitchaichvili, A., Urrutia-Fucugauchi, J., Gonzalez, J.A., Morales, J., Gómez, S., Henríquez, F., Nyström, J.O., and Naslund, R.H., 2003, Rock-magnetic and oxide microscopic studies of the El Laco iron ore deposits, Chilean Andes, and implications for magnetic anomaly modeling: International Geology Review, v. 45, p. 533–547.
- Audétat, A., and Simon, A.C., 2012, Magmatic controls on porphyry Cu genesis: Society of Economic Geologists Special Publication 16, p. 553–572.
- Balan, E., De Vilálbers, J.P., Eeckhout, S.G., Glatzel, P., Toplis, M.J., Fritsch, E., Allard, T., Galois, L., and Calas, G., 2006, The oxidation state of vanadium in titanomagnetite from layered basic intrusions: American Mineralogist, v. 91, p. 953–956.
- Barth, A.P., and Dorais, M.J., 2000, Magmatic anhydrite in granitic rocks: First occurrence and potential petrologic consequences: American Mineralogist, v. 85, p. 430–435.
- Barton, M.D., 2013, Iron oxide(-Cu-Au-REE-P-Ag-U-Co) systems: Treatise on Geochemistry, 2nd ed.: Amsterdam, Elsevier, p. 515–541.
- Bao, B., Webster, J.D., Zhang, D.H., Goldoff, B.A., and Zhang, R.Z., 2016, Compositions of biotite, amphibole, apatite and silicate melt inclusions from the Tongchang mine, Dexing porphyry deposit, SE China: Implications for the behavior of halogens in mineralized porphyry systems: Ore Geology Reviews, v. 79, p. 443–462.
- Bell, A., and Simon, A.C., 2011, Evidence for the alteration of the Fe³⁺/ΣFe of silicate melt caused by the degassing of chlorine-bearing aqueous volatiles: Geology, v. 39, p. 499–502.
- Belousova, E.A., Griffin, W.L., O'Reilly, S.Y., and Fisher, N.I., 2002, Apatite as an indicator mineral for mineral exploration: Trace-element compositions and their relationship to host rock type: Journal of Geochemical Exploration, v. 7, p. 45–69.
- Bilenker, L.D., Simon, A.C., Reich, M., Lundstrom, C.C., Gajos, N., Bindeman, I., Barra, F., and Munizaga, R., 2016, Fe-O stable isotope pairs elucidate a high-temperature origin of Chilean iron oxide-apatite deposits: Geochimica et Cosmochimica Acta, v. 177, p. 94–104.
- Bonyadi, Z., Davidson, G.J., Mehrahi, B., Meffre, S., and Ghazban, F., 2011, Significance of apatite REE depletion and monazite inclusions in the brecciated Se-Chahun iron oxide apatite deposit, Bafq district, Iran: Insights from paragenesis and geochemistry: Chemical Geology, v. 281, p. 253–269.
- Bordage, A., Balan, E., de Villiers, J. P., Cromarty, R., Juhin, A., Carvallo, C., Calas, G., Raju, P.V.S., and Glatzel, P., 2011, V oxidation state in Fe-Ti oxides by high-energy resolution fluorescence-detected X-ray absorption spectroscopy: Physics and Chemistry of Minerals, v. 38, p. 449–458.
- Boudreau, A.E., Love, C., and Prendergast, M.D., 1995, Halogen geochemistry of the Great Dyke, Zimbabwe: Contributions to Mineralogy and Petrology, v. 122, p. 289–300.
- Bouzar, F., Hart, C.J.R., Bissig, T., and Barker, S., 2016, Hydrothermal alteration revealed by apatite luminescence and chemistry: A potential indicator mineral for exploring covered porphyry copper deposits: Economic Geology, v. 111, p. 1397–1410.
- Broman, C., Nyström, J.O., Henríquez, F., and Elfman, M., 1999, Fluid inclusions in magnetite-apatite ore from a cooling magmatic system at El Laco, Chile: GFF, v. 121, p. 253–267.
- Broughm, S.G., Hanchar, J.M., Tornos, F., Westhues, A., and Attersley, S., 2017, Mineral chemistry of magnetite from magnetite-apatite mineralization and their host rocks: Examples from Kiruna, Sweden, and El Laco, Chile: Mineralium Deposita, v. 52, p. 223–244.
- Buddington, A.F., and Lindsley, D.H., 1964, Iron-titanium oxide minerals and synthetic equivalents: Journal of Petrology, v. 5, p. 310–357.
- CAP Minería, 2014, Annual Report, https://www.cap.cl/cap/site/artic/20160512/asocfile/20160512170021/cap_presentacion_larain_vial_marzo_2014.pdf
- Chew, D.M., Babechuk, M.G., Cogné, N., Mark, C., O'Sullivan, G.J., Henrichs, I.A., Doepke, D., and McKenna, C.A., 2016, (LA, Q)-ICPMS trace-element analyses of Durango and McClure Mountain apatite and implications for making natural LA-ICPMS mineral standards: Chemical Geology, v. 435, p. 35–48.
- Childress, T., Simon, A.C., Reich, M., Barra, F., Bilenker, L.D., La Cruz, N.L., Bindeman, I., Ovalle, J.T., 2020, Triple oxygen, hydrogen, and iron stable isotope signatures indicate a silicate magma source and magmatic-hydrothermal genesis for magnetite orebodies at El Laco, Chile: Economic Geology, v. 115, p. 1519–1536.
- Dare, S.A.S., Barnes, S.J., Beaudoin, G., Méric, J., Boutroy, E., and Potvin-Doucet, C., 2014, Trace elements in magnetite as petrogenetic indicators: Mineralium Deposita, v. 49, p. 785–796.
- Dare, S.A.S., Barnes, S.J., and Beaudoin, G., 2015, Did the massive magnetite “lava flows” of El Laco (Chile) form by magmatic or hydrothermal processes? New constraints from magnetite composition by LA-ICP-MS: Mineralium Deposita, v. 50, p. 607–617.
- Dupuis, C., and Beaudoin, G., 2011, Discriminant diagrams for iron oxide trace element fingerprinting of mineral deposit types: Mineralium Deposita, v. 46, p. 319–335.
- Edmonds, M., Brett, A., Herd, R.A., Humphreys, M.C.S. and Woods, A., 2014, Magnetite-bubble aggregates at mixing interfaces in andesite magma bodies: Geological Society (London) Special Publication 410, p. 95–121.

- Giovanninia, A.L., Bastos, A.C., Porto, C.G., Pereira, V.P., Takehara, L., Barbanson, L., and Bastos, P.H.S., 2017, Mineralogy and geochemistry of laterites from the Morro dos Seis Lagos Nb (Ti, REE) deposit (Amazonas, Brazil): *Ore Geology Reviews*, v. 88, p. 461–480.
- Goldoff, B., Webster, J.D., and Harlov, D.E., 2012, Characterization of fluor-chlorapatites by electron probe microanalysis with a focus on time-dependent intensity variation of halogens: *American Mineralogist*, v. 97, p. 1103–1115.
- Groves, D.I., Bierlein, F.P., Meinert, L.D., and Hitzman, M.W., 2010, Iron oxide copper-gold (IOCG) deposits through Earth history: Implications for origin, lithospheric setting, and distinction from other epigenetic iron oxide deposits: *Economic Geology*, v. 105, p. 641–654.
- Gualda, G.A.R., and Ghiorso, M.S., 2007, Magnetite scavenging and the buoyancy of bubbles in magmas. Pt. 2. Energetics of crystal-bubble attachment in magmas: *Contributions to Mineralogy and Petrology*, v. 154, p. 479–490.
- Haggerty, S.E., 1976, Oxidation of opaque mineral oxides in basalts: *Reviews in Mineralogy*, v. 3, p. 1–100.
- 1991, Oxide textures: A mini-atlas: *Reviews in Mineralogy and Geochemistry*, v. 25, p. 129–219.
- Harlov, D.E., 2015, Apatite: A fingerprint for metasomatic processes: *Elements*, v. 11, p. 171–176.
- Harlov, D.E., Andersson, U.B., Förster, H.J., Nyström, J.O., Dulski, P., and Broman, C., 2002, Apatite-monzonite relations in the Kiirunavaara magnetite-apatite ore, northern Sweden: *Chemical Geology*, v. 191, p. 47–72.
- Harlov, D.E., Meighan, C.J., Kerr, I.D., and Samson, I.M., 2016, Mineralogy, chemistry, and fluid-aided evolution of the Pea Ridge Fe oxide-(Y+ REE) deposit, southeast Missouri, USA: *Economic Geology*, v. 111, p. 1963–1984.
- Hedenquist, J.W., and Lowenstern, J.B., 1994, The role of magmas in the formation of hydrothermal ore deposits: *Nature*, v. 370, p. 519.
- Henríquez, F., and Martin, R.F., 1978, Crystal-growth textures in magnetite flows and feeder dykes, El Laco, Chile: *Canadian Mineralogist*, v. 16, p. 581–589.
- Henríquez, F., Naslund, H.R., Nyström, J.O., Vivallo, W., Aguirre, R., Dobbs, F.M., and Lledó, H., 2003, New field evidence bearing on the origin of the El Laco magnetite deposit, northern Chile: *Economic Geology*, v. 98, p. 1497–1500.
- Hughes, J.M., and Rakovan, J.F., 2015, Structurally robust, chemically diverse: apatite and apatite supergroup minerals: *Elements*, v. 11, p. 165–170.
- Hurwitz, S., and Navon, O., 1994, Bubble nucleation in rhyolitic melts: Experiments at high pressure, temperature, and water content: *Earth and Planetary Science Letters*, v. 122, p. 267–280.
- Jochum, K.P., Willbold, M., Raczek, I., Stoll, B., and Herwig, K., 2005, Chemical characterisation of the USGS Reference Glasses GSA-1G, GSC-1G, GSD-1G, GSE-1G, BCR-2G, BHVO-2G and BIR-1G using EPMA, ID-TIMS, ID-ICP-MS and LA-ICP-MS: *Geostandards and Geoanalytical Research*, v. 29, p. 285–302.
- Jochum, K.P., Weis, U., Stoll, B., Kuzmin, D., Yang, Q., Raczek, I., Jacob, D.E., Stracke, A., Birbaum, K., Frick, D.A., and Günther, D., 2011, Determination of reference values for NIST SRM 610-617 glasses following ISO guidelines: *Geostandards and Geoanalytical Research*, v. 35, p. 397–429.
- Jonsson, E., Harlov, D.E., Majka, J., Högdahl, K., and Persson-Nilsson, K., 2016, Fluorapatite-monzonite-allanite relations in the Grängesberg apatite-iron oxide ore district, Bergslagen, Sweden: *American Mineralogist*, v. 101, p. 1769–1782.
- Kempe, U., and Götze, J., 2002, Cathodoluminescence (CL) behaviour and crystal chemistry of apatite from rare-metal deposits: *Mineralogical Magazine*, v. 66, p. 151–172.
- Ketcham, R.A., 2015, Technical Note: Calculation of stoichiometry from EMP data for apatite and other phases with mixing on monovalent anion sites: *American Mineralogist*, v. 100, p. 1620–1623. doi:10.2138/am-2015-5171
- Knipping, J.L., Bilénker, L.D., Simon, A.C., Reich, M., Barra, F., Deditius, A.P., Lundström, C., Bindeman, I., and Munizaga, R., 2015a, Giant Kiruna-type deposits form by efficient flotation of magmatic magnetite suspensions: *Geology*, v. 43, p. 591–594.
- Knipping, J.L., Bilénker, L.D., Simon, A.C., Reich, M., Barra, F., Deditius, A.P., Wälle, M., Heinrich, C.A., Holtz, F., and Munizaga, R., 2015b, Trace elements in magnetite from massive iron oxide-apatite deposits indicate a combined formation by igneous and magmatic-hydrothermal processes: *Geochimica et Cosmochimica Acta*, v. 171, p. 15–38.
- Knipping, J.L., Webster, J.D., Simon, A.C., and Holtz, F., 2019, Accumulation of magnetite by flotation on bubbles during decompression of silicate magma: *Scientific Reports*, v. 9, p. 3852. doi.org/10.1038/s41598-019-40376-1
- Konecke, B.A., Fiege, A., Simon, A.C., Parat, F., and Stechern, A., 2017a, Co-variability of S^{6+} , S^{4+} and S^{2-} in apatite as a function of oxidation state: Implications for a new oxybarometer: *American Mineralogist*, v. 102, p. 548–557. doi:10.2138/am-2017-5907
- Konecke, B., Fiege, A., Simon, A.C., and Holtz, F., 2017b, Cryptic metasomatism during late-stage lunar magmatism implicated by sulfur in apatite: *Geology*, v. 45, p. 739–742.
- Krneta, S., Ciobanu, C.L., Cook, N.J., Ehrig, K., and Kontonikas-Charos, A., 2016, Apatite at Olympic Dam, South Australia: A petrogenetic tool: *Lithos*, v. 262, p. 470–485.
- La Cruz, N.L., Simon, A.C., Wolf, A.S., Reich, M., Barra, F., and Gagnon, J.E., 2019, The geochemistry of apatite from the Los Colorados iron oxide-apatite deposit, Chile: Implications for ore genesis: *Mineralium Deposita*, p. 1–14. doi.org/10.1007/s00126-019-00861-z
- Lester, G.W., Kyser, T.K., and Clark, A.H., 2013a, Oxygen isotope partitioning between immiscible silicate melts with H_2O , P and S: *Geochimica et Cosmochimica Acta*, v. 109, p. 306–311.
- Lester, G.W., Clark, A.H., Kyser, T.K., and Naslund, H.R., 2013b, Experiments on liquid immiscibility in silicate melts with H_2O , P, S, F and Cl: Implications for natural magmas: *Contributions to Mineralogy and Petrology*, v. 166, p. 329–349.
- Lindsley, D.H., 1962, Investigations in the system $FeO-Fe_2O_3-TiO_2$: *Carnegie Institute of Washington Yearbook*, v. 61, p. 100–106.
- 1963, Equilibrium relations of coexisting pairs of Fe-Ti oxides: *Carnegie Institute of Washington Yearbook*, v. 62, p. 60–66.
- 1991, Experimental studies of oxide minerals: *Reviews in Mineralogy*, v. 25, p. 69–106.
- Longerich, H.P., Jackson, S.E., and Günther, D., 1996, Inter-laboratory note. Laser ablation inductively coupled plasma mass spectrometric transient signal data acquisition and analyte concentration calculation: *Journal of Analytical Atomic Spectrometry*, v. 11, p. 899–904.
- Maksaev, V., Gardeweg, M., Ramírez, C.F., and Zentilli, M., 1988, Aplicación del método trazas de fisión (fission track) a la datación de cuerpos de magnetita de El Laco e Incahuasi en el altiplano de la Región de Antofagasta: *Congreso Geológico Chileno*, no. 5, p. B1–B24.
- Mao, M., Rukhlov, A.S., Rowins, S.M., Spence, J., and Coogan, L.A., 2016, Apatite trace element compositions: A robust new tool for mineral exploration: *Economic Geology*, v. 111, p. 1187–1222.
- Marks, M.A., Wenzel, T., Whitehouse, M.J., Loose, M., Zack, T., Barth, M., Worgard, L., Krasz, V., Eby, G.N., Stosnach, H., and Markl, G., 2012, The volatile inventory (F, Cl, Br, S, C) of magmatic apatite: An integrated analytical approach: *Chemical Geology*, v. 291, p. 241–255.
- Marsh, B.D., 1989, Magma chambers: *Annual Reviews of Earth and Planetary Science*, v. 17, p. 439–474.
- Martel, C., Pichavent, M., Holtz, F., and Scaillet, B., 1999, Effects of f_{O_2} and H_2O on andesite phase relations between 2 and 4 kbar: *Journal of Geophysical Research*, v. 104, p. 29453–29470.
- Mungall, J.E., Long, K., Brennan, J.M., Smythe, D., and Naslund, H.R., 2018, Immiscible shoshonitic and Fe-P-oxide melts preserved in unconsolidated tephra at El Laco volcano, Chile: *Geology*, v. 46, p. 255–258.
- Nadoll, P., Angerer, T., Mauk, J.L., French, D., and Walshe, J., 2014, The chemistry of hydrothermal magnetite: A review: *Ore Geology Reviews*, v. 61, p. 1–32.
- Naranjo, J.A., Henríquez, F., and Nyström, J.O., 2010, Subvolcanic contact metasomatism at El Laco Volcanic Complex, Central Andes: *Andean Geology*, v. 37, p. 110–120.
- Naslund, H.R., Dobbs, F.M., Henríquez, F.J., and Nyström, J.O., 1997, Irrefutable evidence for the eruption of iron-oxide magmas at El Laco Volcano, Chile: *EOS*, v. 78, p. S333.
- 1998, Evidence for iron-oxide magmas at El Laco, Chile: *Geological Society of America Abstracts with Programs*, v. 30, p. 91.
- Naslund, H.R., Henríquez, F., Nyström, J.O., Vivallo, W., and Dobbs, F.M., 2002, Magmatic iron ores and associated mineralization: Examples from the Chilean High Andes and Coastal Cordillera, in: Porter, T.M., ed., *Hydrothermal iron oxide copper-gold and related deposits: A global perspective*, 2nd ed.: Adelaide, PGC Publishing, p. 207–226.
- Nielsen, R.L., Forsythe, L.M., Gallahan, W.E., and Fisk, M.R., 1994, Major- and trace-element magnetite-melt equilibria: *Chemical Geology*, v. 117, p. 167–191.
- Normandeau, P.X., Harlov, D.E., Corriveau, L., Paquette, J., and McMartin, I., 2018, Characterization of fluorapatite within iron oxide alkali-calcic alteration systems of the Great Bear magmatic zone: A potential metasomatic process record: *Canadian Mineralogist*, v. 56, p. 167–187.

- Nyström, J.O., and Henríquez, F., 1994, Magmatic features of iron ores of the Kiruna type in Chile and Sweden: Ore textures and magnetite geochemistry: *Economic Geology*, v. 89, p. 820–839.
- Ovalle, J.T., La Cruz, N.L., Reich, M., Barra, F., Simon, A.C., Konecke, B.A., Rodríguez-Mustafa, M.A., Deditius, A.P., Childress, T.M., and Morata, D., 2018, Formation of massive iron deposits linked to explosive volcanic eruptions: *Scientific Reports*, v. 8, p. 1–11.
- Oyarzun, J., and Frutos, J., 1984, Tectonic and petrological frame of the Cretaceous iron deposits of north Chile: *Mining Geology*, v. 34, p. 21–31.
- Palma, G., Barra, F., Reich, M., Valencia, V., Simon, A.C., Vervoort, J., Leisen, M., and Romero, R., 2019, Halogens (F, Cl, OH), trace element contents, and Sr-Nd isotopes in apatite from iron oxide-apatite (IOA) deposits in the Chilean iron belt: Evidence for magmatic and hydrothermal stages of mineralization: *Geochimica et Cosmochimica Acta*, v. 246, p. 515–540.
- Parat, F., Holtz, F., and Streck, M.J., 2011, Sulfur-bearing magmatic accessory minerals: Reviews in Mineralogy and Geochemistry, v. 73, p. 285–314.
- Park, C.F., 1961, A magnetite "flow" in northern Chile: *Economic Geology*, v. 56, p. 431–436.
- Patiño Douce, A.E.P., Roden, M.F., Chaumba, J., Fleisher, C., and Yogodzinski, G., 2011, Compositional variability of terrestrial mantle apatites, thermodynamic modeling of apatite volatile contents, and the halogen and water budgets of planetary mantles: *Chemical Geology*, v. 288, p. 14–31.
- Paton, C., Hellstrom, J., Paul, B., Woodhead, J., and Hergt, J., 2011, Iolite: Freeware for the visualisation and processing of mass spectrometric data: *Journal of Analytical Atomic Spectrometry*, v. 26, p. 2508–2518.
- Piccoli, P.M., and Candela, P.A., 2002, Apatite in igneous system: Reviews in Mineralogy and Geochemistry, v. 48, p. 255–292.
- Pleše, P., Higgins, M.D., Baker, D.R., Lanzafame, G., Kudrna Prašek, M., Mancini, L., and Rooyakkers, S.M., 2019, Production and detachment of oxide crystal shells on bubble walls during experimental vesiculation of andesitic magmas: Contributions to Mineralogy and Petrology, v. 174, p. 21. doi.org/10.1007/s00410-019-1556-8
- Reed, M.J., Candela, P.A., and Piccoli, P.M., 2000, The distribution of rare earth elements between monzogranitic melt and the aqueous volatile phase in experimental investigations at 800°C and 200 MPa: Contributions to Mineralogy and Petrology, v. 140, p. 251–262.
- Rhodes, A.L., and Oreskes, N., 1995, Magnetite deposition at El Lago, Chile: Implications for Fe-oxide formation in magmatic-hydrothermal systems, in Clark, A.H., ed., Giant ore deposits-II: Controls on the scale of orogenic magmatic-hydrothermal mineralization. Proceedings of the Second Giant Ore Deposits Workshop: Kingston, Queen's University, p. 582–622.
- 1999, Oxygen isotope composition of magnetite deposits at El Lago, Chile: Evidence of formation from isotopically heavy fluids: Society of Economic Geology Special Publication 7, p. 333–351.
- Rhodes, A.L., Oreskes N., and Sheets S., 1999, Geology and rare earth element geochemistry of magnetite deposits at El Lago, Chile: Society of Economic Geology Special Publication 7, p. 299–332.
- Rojas, P.A., Barra, F., Deditius, A., Reich, M., Simon, A., Roberts, M., and Rojo, M., 2018, New contributions to the understanding of Kiruna-type iron oxide-apatite deposits revealed by magnetite ore and gangue mineral geochemistry at the El Romeral deposit, Chile: *Ore Geology Reviews*, v. 93, p. 413–435.
- Rudnick, R.L., and Gao, S., 2003, Composition of the continental crust: Treatise on Geochemistry, v. 3, p. 659.
- Sadove, G., Konecke, B., Fiege, A., and Simon, A. C., 2019, Structurally bound S2–, S1–, S4+, S6+ in terrestrial apatite: The redox evolution of hydrothermal fluids at the Phillips mine, New York, USA: *Ore Geology Reviews*, v. 107, p. 1084–1096.
- Salazar, E., Barra, F., Reich, M., Simon, A.C., Leisen, M., Palma, G., Romero, R., and Rojo, M., 2019, Trace-element geochemistry of magnetite from the Cerro Negro Norte iron oxide-apatite deposit, northern Chile: *Mineralium Deposita*, v. 55, p. 409–428. https://doi.org/10.1007/s00126-019-00879-3
- Schettler, G., Gottschalk, M., and Harlov, D.E., 2011, A new semi-micro wet chemical method for apatite analysis and its application to the crystal chemistry of fluorapatite-chlorapatite solid solutions: *American Mineralogist*, v. 96, p. 138–152.
- Sillitoe, R.H., and Burrows, D.R., 2002, New field evidence bearing on the origin of the El Lago magnetite deposit, northern Chile: *Economic Geology*, v. 97, p. 1101–1109.
- Simon, A.C., and Ripley, E.M., 2011, The role of magmatic sulfur in the formation of ore deposits: Reviews in Mineralogy and Geochemistry, v. 73, p. 513–578.
- Simon, A.C., Pettke, T., Candela, P.A., Piccoli, P.M., and Heinrich, C.A., 2004, Magnetite solubility and iron transport in magmatic-hydrothermal environments: *Geochimica et Cosmochimica Acta*, v. 68, p. 4905–4914.
- Simon, A.C., Pettke, T., Candela, P.A., Piccoli, P.M., and Heinrich, C.A., 2007, The partitioning behavior of As and Au in S-free and S-bearing magmatic assemblages: *Geochimica et Cosmochimica Acta*, v. 71, p. 1764–1782.
- Simon, A.C., Knipping, J., Reich, M., Barra, F., Deditius, A.P., Bilenker, L., and Childress, T., 2018, Kiruna-type iron oxide-apatite (IOA) and iron oxide copper-gold (IOCG) deposits form by a combination of igneous and magmatic-hydrothermal processes: Evidence from the Chilean iron belt: Society of Economic Geologists Special Publication 21, p. 89–114.
- Stromer, J.C., Pierson, M.L., and Tacker, R.C., 1993, Variation of F and Cl X-ray intensity due to anisotropic diffusion in apatite during electron microprobe analysis: *American Mineralogist*, v. 78, p. 641–648.
- Streck, M.J., and Dilles, J.H., 1998, Sulfur evolution of oxidized arc magmas as recorded in apatite from a porphyry copper batholith: *Geology*, v. 26, p. 523–526.
- Taghipour, S., Kananian, A., Harlov, D., and Oberhänsli, R., 2015, Kiruna-type iron oxide-apatite deposits, Bafq district, central Iran: Fluid-aided genesis of fluorapatite-monzonite-xenotime assemblages: *Canadian Mineralogist*, v. 53, p. 479–496.
- Toplis, M.J., and Carroll, M.R., 1995, An experimental study of the influence of oxygen fugacity on Fe-Ti oxide stability, phase relations, and mineral-melt equilibria in ferro-basaltic systems: *Journal of Petrology*, v. 36, p. 1137–1170.
- Torab, F.M., and Lehmann, B., 2007, Magnetite-apatite deposits of the Bafq district, Central Iran: Apatite geochemistry and monazite geochronology: *Mineralogical Magazine*, v. 71, p. 347–363.
- Tornos, F., Velasco, F., and Hanchar, J.M., 2016, Iron-rich melts, magmatic magnetite, and superheated hydrothermal systems: The El Lago deposit, Chile: *Geology*, v. 44, p. 427–430.
- 2017, The magmatic to magmatic-hydrothermal evolution of the El Lago deposit (Chile) and its implications for the genesis of magnetite-apatite deposits: *Economic Geology*, v. 112, p. 1595–1628.
- Treloar, P.J., and Colley, H., 1996, Variation in F and Cl contents in apatites from magnetite-apatite ores in northern Chile, and their ore-genetic implications: *Mineralogical Magazine*, v. 60, p. 285–301.
- Tucker, P., and O'Reilly, W., 1980, The laboratory simulation of deuteric oxidation of titanomagnetites: Effect on magnetite properties and stability of thermoremanence: *Physics of the Earth and Planetary Interiors*, v. 23, p. 112–133.
- Velasco, F., Tornos, F., and Hanchar, J.M., 2016, Immiscible iron- and silica-rich melts and magnetite geochemistry at the El Lago volcano (northern Chile): Evidence for a magmatic origin for the magnetite deposits: *Ore Geology Reviews*, v. 79, p. 346–366.
- Vivallo, W., Henríquez, F., and Espinoza, S., 1994, Oxygen and sulfur isotopes in hydrothermally altered rocks and gypsum deposits at El Lago mining district, northern Chile: *Comunicaciones, Departamento de Geología, Universidad de Chile, Santiago*, v. 45, p. 93–100.
- Webster, J.D., and Piccoli, P.M., 2015, Magmatic apatite: A powerful, yet deceptive, mineral: *Elements*, v. 11, p. 177–182.
- Wen, G., Li, J.W., Hofstra, A.H., Koenig, A.E., Lowers, H.A., and Adams, D., 2017, Hydrothermal reequilibration of igneous magnetite in altered granitic plutons and its implications for magnetite classification schemes: Insights from the Handan-Xingtai iron district, North China craton: *Geochimica et Cosmochimica Acta*, v. 213, p. 255–270.
- Williams, P.J., Barton, M.D., Johnson, D.A., Fontboté, L., De Haller, A., Mark, G., Oliver, N.H., and Marschik, R., 2005, Iron oxide copper-gold deposits: Geology, space-time distribution, and possible modes of origin: *Economic Geology 100th Anniversary Volume*, p. 371–405.
- Williams-Jones, A.E., and Heinrich, C.A., 2005, Vapor transport of metals and the formation of magmatic-hydrothermal ore deposits: *Economic Geology 100th Anniversary Volume*, p. 1287–1312.
- Xie, Q., Zhang, Z., Hou, T., Cheng, Z., Campos, E., Wang, Z. and Fei, X., 2019, New insights for the formation of Kiruna-type iron deposits by immiscible hydrous Fe-P melt and high-temperature hydrothermal processes: Evidence from El Lago deposit: *Economic Geology*, v. 114, p. 35–46.
- Xu, W., Van der Voo, R., Peacor, D.R., and Beaubouef, R.T., 1997, Alteration and dissolution of fine-grained magnetite and its effects on magnetization of the ocean floor: *Earth and Planetary Science Letters*, v. 151, p. 279–288.

Nikita L. La Cruz is an economic geologist who completed her Ph.D. at the University of Michigan in September 2019. She received B.Sc. degrees in chemistry and environmental studies at Gettysburg College in 2013, and an M.Sc. degree in geology with a focus in geochemistry at University of South Florida in 2015. She is currently a senior geologist at the Guyana Geology and Mines Commission, where she is actively working to understand the geology and ore deposit potential of Guyana. Prior to completion of her Ph.D., Nikita worked in greenfield exploration in Guyana.



